Superconductivity in atomically thin films: Two-dimensional critical state model

Filippo Gaggioli,[1] Gianni Blatter,[1] Kostya S. Novoselov,[2] and Vadim B. Geshkenbein[1]
[1]*Institut für Theoretische Physik, ETH Zürich, CH-8093 Zürich, Switzerland*
[2]*Institute for Functional Intelligent Materials, National University of Singapore, Singapore 117544, Singapore*

(Received 12 February 2024; revised 3 April 2024; accepted 9 April 2024; published 20 May 2024)

The comprehensive understanding of superconductivity is a multiscale task that involves several levels, starting from the electronic scale determining the microscopic mechanism, going to the phenomenological scale describing vortices and the continuum-elastic scale describing vortex matter, to the macroscopic scale relevant in technological applications. The prime example for such a macro-phenomenological description is the Bean model that is hugely successful in describing the magnetic and transport properties of bulk superconducting devices. Motivated by the development of novel devices based on superconductivity in atomically thin films, such as twisted-layer graphene, here, we present a simple macro-phenomenological description of the critical state in such two-dimensional (2D) thin films. While transverse screening and demagnetization can be neglected in these systems, thereby simplifying the task in comparison with usual film- and platelet-shaped samples, surface and bulk pinning are important elements to be included. We use our 2D critical state model to describe the transport and magnetic properties of 2D thin-film devices, including the phenomenon of nonreciprocal transport in devices with asymmetric boundaries and the superconducting diode effect.

DOI: 10.1103/PhysRevResearch.6.023190

I. INTRODUCTION

Technologically relevant superconductors are usually type II materials, with vortices determining their phenomenological properties [1]. In technical applications, the material is often described through its macro-phenomenological properties where vortices appear as an effective medium rather than individual objects. The first such description was the Bean model [2] that describes magnetic and transport properties of bulk material in terms of the critical current density $j_p(B)$ due to bulk pinning [3], the latter taking the role of a constitutive material relation (here, B denotes the magnetic induction that is related to the vortex density $n = 1/a_0^2 = B/\Phi_0$, $\Phi_0 = hc/2e$ is the superconducting flux quantum, and a_0 the vortex separation). A second type of macro-phenomenological description applies to flat samples, e.g., films and platelet-shaped samples as they appeared with the then-novel cuprate superconductors in the late eighties and nineties. Besides bulk pinning [3], surface pinning [4–7], geometric barriers [7–10], and demagnetization phenomena [7,11–13] become relevant. Today, much interest is focused on atomically thin van der Waals materials [14,15] with superconducting properties [16], as found in transition metal dichalcogenides [17,18] and twisted-layer graphene [19,20]. While significant efforts have focused on explaining the microscopic aspects of superconductivity in such atomically thin materials [16,21–23], less emphasis has been devoted to studying the phenomenology of these systems. In the present paper, we introduce a third kind of macro-phenomenological model that describes the two-dimensional (2D) critical state of atomically thin superconductors and use it to determine the relevant transport and magnetic properties of these materials.

Atomically thin superconductors can easily be tuned, a feature owed to their nanometric thickness. For example, the surface barrier can be manipulated not only via the geometric design of the edges [24], but also via a finite gate voltage [25]. In a recent paper, the interplay between vortex pinning, the moiré pattern in $NbSe_2$ layers, and the effects of a perpendicular electric field has been studied [26], demonstrating the expanded toolkit for engineering superconductivity in this type of materials. This high degree of tunability makes 2D superconductors an ideal platform for realizing interesting and novel devices, see for example the numerous reports on the so-called superconducting diode effect [26–43]. One important goal of this paper then is to provide a simple macro-phenomenological model capable of describing the properties of these 2D materials and their physical performance in technical applications.

The Bean model has been hugely successful in explaining the magnetic and transport properties of the mixed state in bulk material. It reduces the complex pinning behavior of the vortex matter to a simple constitutive material relation $j_p(B)$. In its simplest (original) variant, j_p is assumed to be independent on the B field (i.e., the vortex density n; we assume $\mathbf{B} \parallel \mathbf{z}$) and solving Maxwell-Ampère's equation $\nabla \wedge \mathbf{B} = (4\pi/c)\,\mathbf{j}_p$ provides the magnetic response of a bulk sample as shown in Fig. 1(a), i.e., the current and vortex densities $j(x)$ and $n(x) = B(x)/\Phi_0$ across the superconductor (we assume a finite-width sample along x and an infinite extension along y). The simplest critical state is characterized by a constant

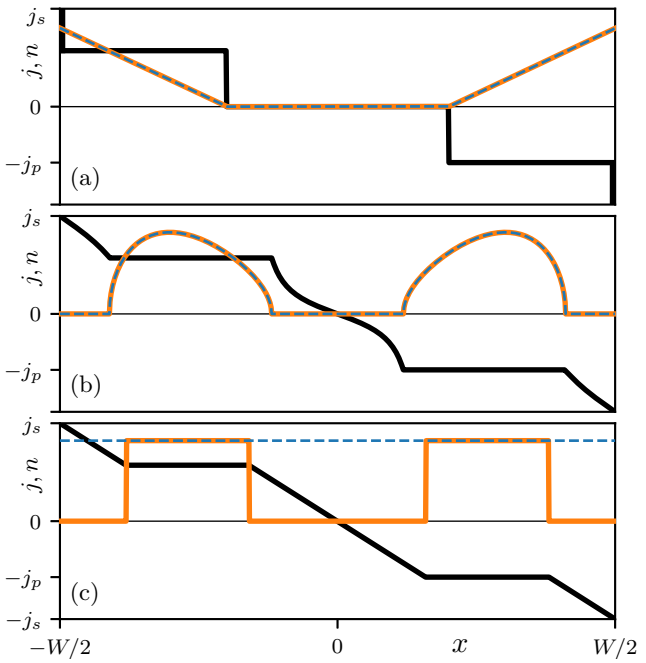

FIG. 1. Illustration of the critical state (partial penetration) for three types of sample geometries, bulk (a), flat samples (b), and 2D thin films (c), in a (perpendicular) magnetic field $\mathbf{H} \parallel \mathbf{z}$. Current and vortex densities $j(x)$ and $n(x)$ are shown as black and orange lines (j_s and j_p denote surface and bulk critical current densities); the corresponding field distribution $B(x)$ is shown as a blue dashed line. (a) Bean model [2] describing bulk samples. (b) Flat sample, e.g., a film- or platelet-shaped superconductor, with large demagnetization effects [12,13] and vortices arranging in a pair of domes inside the sample [8]. (c) In 2D thin-film superconductors, screening can be neglected and the magnetic field penetrates homogeneously, with constant $B \approx H$ everywhere. While in (a), the bulk critical current density j_p is the dominating parameter, it is the surface critical current density j_s that determines the critical state in (c). Comparing (b) and (c), the density profiles $j(x)$ and $n(x)$ differ only quantitatively but the field profiles $B(x)$ turn out very different.

current density $j = j_p$ in the penetrated part of the sample that is associated with a linear decrease in (pinned) vortex density $n(x)$ away from the sample surface, while both current and vortex densities vanish inside. Increasing the external field H, the vortices penetrate to the middle of the sample (state of full penetration) and the screening saturates with the magnetization $M = -j_p W/4c$. Accounting for surface effects, vortex entry into the sample is delayed due to the surface barrier, with Meissner currents flowing on a scale $\sim a_0^2/\xi > a_0$ at the boundaries defining a vortex-free region [5,7].

With the emergence of high-temperature superconductors, numerous studies have focused on the phenomenological properties arising from their platelet/film geometry with typical film thickness d larger than the London penetration depth λ. We separate such "flat samples" with $d \gg \lambda$ from the "two-dimensional (2D) thin films" with $d \ll \lambda$, the geometry we will focus on in the present paper, see below. Placing a flat sample ($d \gg \lambda$) in a perpendicular magnetic field, i.e., with the shortest dimension d parallel to the external field $\mathbf{H} \parallel \mathbf{z}$, demagnetization effects are strong and the field lines bend around the sample, resulting in Meissner screening currents flowing along all sample boundaries including the top and bottom surfaces perpendicular to the field [12,13]. Furthermore, surface and geometric edge effects [5–9] determine the field where vortices penetrate into the sample. In Fig. 1(b), we illustrate the resulting critical state in flat samples involving Meissner- and vortex-related current densities: since Meissner currents flow on all sample boundaries [8,12,13], vortices are pushed into the sample as soon as the surface/geometrical barrier is overcome; they form two isolated vortex domes where currents $j = \pm j_p$ flow due to bulk pinning. Meissner currents outside these domes seemingly diverge at the film boundaries (they are cut off at distance d from the edge) and connect the vortex-pinning-induced current plateaus across the film center. The magnetic field in the z direction (evaluated in the film middle at $z = 0$) vanishes everywhere due to Meissner screening currents, except for the inside of vortex domes and the thin λ layer at the edges (note the difference between the domes in Fig. 1(b) and the corresponding results in Refs. [12,13], which is due to the missing of the geometrical barrier in this early study on flat samples: the large Meissner currents at the edges drive vortices, that have overcome the geometrical barrier, to the inside of the film). Hence, a rich critical-state phenomenology (involving conformal mappings and theory of analytic functions in the underlying mathematics [7,8,44,45]) characterizes the analysis of flat superconductors that goes beyond the simple description of bulk pinning within the Bean model.

The critical state in 2D thin films with $d \ll \lambda$ is characterized by the weakness of superconducting screening: As the film thickness d drops below the bulk penetration depth λ, the effective screening length is given by the Pearl length $\lambda_\perp = 2\lambda^2/d$ [46]. For thicknesses d in the nanometric range, typical of atomically thin devices, the effective penetration depth $\lambda_\perp$ is much larger than the coherence length ξ, bringing these materials under the type II paradigm. Even more, $\lambda_\perp$ easily exceeds the film width W, $\lambda_\perp \gg W$, and the magnetic field remains unscreened, with $B \approx H$ throughout the film width. This then defines the parametric regime that we focus on in the present paper: 2D thin films with thickness $d \ll \lambda$ and a finite width W such that $\lambda_\perp \gg W$. This results in the absence of screening and demagnetization effects and allows us to formulate a simple theory for the critical state of such 2D thin-film material that departs significantly from its counterpart in bulk and flat samples, see Fig. 1(c). Note that a similar absence of screening characterizes the situation of a thin film with $d < \lambda$ in the parallel-field geometry, see Refs. [47,48].

While demagnetization and screening can be ignored in 2D thin films with $d \ll \lambda$, both surface- and bulk-pinning effects play important roles and we will briefly discuss both, one after the other. The vanishing of the current density $j_\perp$ at the film boundary generates a *surface barrier* for vortex entry (conveniently described by a fictitious image vortex of opposite circulation) that allows for a surface current density j_s of order of the depairing current density $j_0 \equiv c\Phi_0/12\sqrt{3}\pi^2\lambda^2\xi$ to flow at a distance $\lambda_\perp$ from the boundaries, i.e., everywhere inside the sample in a typical situation where $\lambda_\perp \gg W$. Combining Maxwell-Ampère's and London's equation $\mathbf{j} = -(c/2\pi\lambda_\perp)\mathbf{A}$ (where $\mathbf{A}$ is the vector potential associated with the induction $\mathbf{B}$) then tells us that the current changes

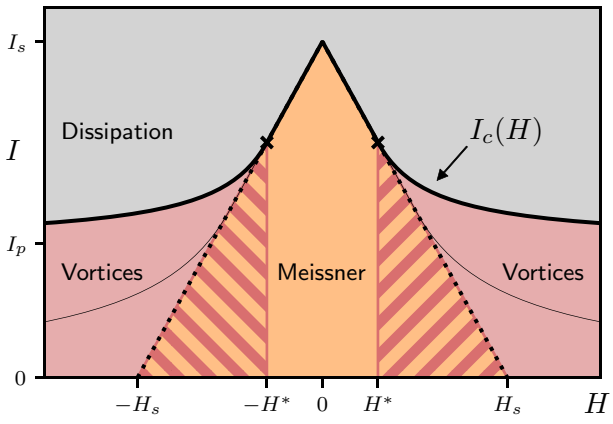

FIG. 2. Critical current $I_c(H)$ (black-solid line) and hysteretic diagram (colors) for a 2D thin-film superconductor in a perpendicular magnetic field H. The critical current $I_c(H)$ provides the maximal dissipation-free current supported by the superconducting film. At small fields $|H| \leqslant H^*$, the critical current is determined by the surface pinning inhibiting vortex entry at the sample boundary, with $I_c(|H| \leqslant H^*)$ decreasing linearly, see (16). For fields beyond H^*, the critical current $I_c(|H| > H^*)$ is limited by vortex motion and decays $\propto 1/|H|$ before saturating at the bulk pinning current I_p, see (17). Upon increasing the current from zero at fixed H, vortices enter the film for currents $I > I_s(H) = I_s(1 - |H|/H_s)$ [black-dotted line, see (19)] that delimits the Meissner state (orange) on increasing currents. Decreasing the current below $I_c(H)$ at fixed $|H| > H^*$, the film enters the mixed state (red and red stripes). In the absence of bulk pinning, $H^* = H_s/2$ and $I_c(|H| > H^*) = I_s H_s/4|H|$ (thin-solid line).

linearly $\propto -H$ inside the film as long as H remains small, $H < H_s \propto j_s$. Pushing the external field H beyond the surface penetration field H_s drives the current density j at the boundaries beyond j_s and vortices enter the film. These are driven towards the film center where they accumulate in the shape of a rectangular box, a "plateau" replacing the "dome" in flat samples [8] of width $d \gg \lambda$. As the vortex box expands with further increasing magnetic field H, the surface current is squeezed to a narrow layer that reaches the width ξ at the scale of the upper critical field H_{c2}.

In the presence of *"bulk" pinning* with a finite critical current density $j_p > 0$, vortices are driven towards the thin-film center as long as the local current density j stays larger then j_p. Hence, a symmetric pair of vortex boxes appear away from the boundaries within the 2D thin film as illustrated in Fig. 1(c); they expand with increasing drive H and reach the film center (to scale a_0) at the full-penetration field $\sim(j_p/j_0)^2 H_{c2}$. As a result, the critical state in 2D thin films differs considerably from those in bulk and flat samples. Particularly noteworthy is the exchange of constant and linear dependencies in the field- and current traces when going between the bulk and the 2D critical states, see Figs. 1(a) and 1(c).

Extending the above critical-state analysis in 2D thin films to include transport currents I, we can calculate the critical current $I_c(H)$ of devices in the presence of magnetic fields H as shown in Fig. 2. We find that the large currents associated with the surface barrier dominate the current flow and determine the linear field dependence [27,49,50] of the critical current $I_c(H) - I_c(0) \propto |H|$ at small magnetic fields $|H| \leqslant H^*$ before vortex entry ($H^* = H_s/2$ in the absence of bulk pinning), see the solid-black line in Fig. 2. At larger fields, vortices occupy a large part of the sample and $I_c(H)$ decreases nonlinearly to a saturation value determined by the bulk critical current density j_p. The figure also informs about the different phases that appear in 2D thin films at given values of field H and current I, dissipative (grey), Meissner (orange), and mixed (red); the latter two, Meissner versus mixed states depend on the preparation of the state, here shown is the result of increasing (decreasing) the current I from zero [from $I_c(H)$] at fixed H. A further extension of the model to account for unequal surfaces in asymmetric devices leads us to nonreciprocal transport that is the basis for the superconducting diode effect.

In this paper, we build on previous studies [27,49,50] to provide an exhaustive description of the 2D critical state model of 2D thin-film superconductors with thickness $d \ll \lambda$. In Sec. II, we introduce the 2D critical state model for such 2D thin films based on the Maxwell-London equation that governs the current distribution across such films. We work in the limit $W \ll \lambda_\perp$ typical of atomically thin strips where we can neglect effects of screening, while fully accounting for both surface and bulk vortex pinning. We make use of this 2D critical state model to calculate vortex, as well as current density profiles, first in a finite field without transport, see Sec. II A, that leads us to Fig. 1(c). In Sec. II B, we determine the field H dependence of the critical current $I_c(H)$, see Fig. 2, and then find the critical state for a transport current $0 < I < I_c(H)$ in between. In Sec. III, we determine the nonreciprocal transport properties of asymmetric devices and discuss the superconducting diode effect. We find (in Sec. III A) that the critical current $I_c(H)$ reaches its maximum at a finite-peak field $H_{\rm max}$. The different critical currents for positive and negative currents then give rise to the superconducting diode effect. Including bulk pinning, we find an upper bound on the diode efficiency $\eta(H)$ of the 2D thin film even in strongly asymmetric devices, see Sec. III B. In Sec. III C, we compare our critical state predictions with recent experiments. While a great deal of transport measurements have been reported on atomically thin superconductors, not much attention has been paid to the magnetic properties of these materials. In the final part of this paper, see Sec. IV, we use our 2D critical state model to determine the hysteretic moment $m(H)$ that exhibits numerous features generated by the interplay of surface and bulk pinning. Besides strong experimental signatures, such as kinks, we find a rich variety of vortex configurations such as vortex–antivortex coexistence fronts inside the sample. Section V summarizes our results and provides some conclusions.

II. 2D CRITICAL STATE MODEL

We consider a thin ($d \ll \lambda$) superconducting film (in the $x - y$ plane) in a perpendicular magnetic field $\mathbf{H} = H\hat{\mathbf{z}}$. Inside the superconductor, the current density distribution $\mathbf{j}$ is determined self-consistently by the interplay of the external field $\mathbf{H}$, the distribution of superconducting vortices and the self-field $\mathbf{B}_{\rm self}$ induced by the current density $\mathbf{j}$, as given by the Biot-Savart integral. Our 2D thin film has a finite width $-W/2 \leqslant x \leqslant W/2$ along x and extends to infinity along y. For a film of thickness d smaller than the London length λ,

the current density $\mathbf{j}(\mathbf{R})$ is homogeneous in the field direction z and we define the sheet current density $\mathbf{i}(\mathbf{R}) \equiv \mathbf{j}(\mathbf{R})d$ that depends on the position $\mathbf{R}$ within the plane of the film. The sheet current density $\mathbf{i}(\mathbf{R})$ is related to the electromagnetic vector potential $\mathbf{A}(\mathbf{r})$ and the condensate phase $\theta(\mathbf{R})$ through the London equation

$$\mathbf{i}(\mathbf{R}) = -\frac{cd}{4\pi\lambda^2}\left[\mathbf{A}(\mathbf{R}, z=0) - \frac{\Phi_0}{2\pi}\nabla\theta(\mathbf{R})\right]. \tag{1}$$

We take the curl of Eq. (1) and rewrite the total field $\mathbf{B} = \nabla \times \mathbf{A}$ as the sum of the external and Biot-Savart fields $\mathbf{H}$ and $\mathbf{B}_{\rm self}(\mathbf{r})$; furthermore, we replace the singular gauge part $\nabla \times [\nabla\theta(\mathbf{R})] = 2\pi\hat{\mathbf{z}}\sum_n \delta(\mathbf{R} - \mathbf{R}_n)$ by the vortex density $\hat{\mathbf{z}}n(\mathbf{R})$. This approximation is an integral part of our macro-phenomenological description where we are interested in scales larger than the intervortex separation. Accounting for the film geometry and boundary conditions (infinite extension and current along y), the z component of the curl provides us with the Maxwell-London equation [51] for the sheet current density $i(x) \equiv i_y(x)$,

$$\frac{d\,i}{d\,x} = -\frac{cd}{4\pi\lambda^2}[H - n(x)\Phi_0 + B_{\rm self}(x)], \tag{2}$$

with the z component of the self-field

$$B_{\rm self}(x) = \frac{2}{c}\int_{-W/2}^{W/2} \frac{i(x')\,dx'}{x' - x}. \tag{3}$$

Equation (2) defines an integrodifferential equation for $i(x)$ with a characteristic length scale $\lambda_\perp = 2\lambda^2/d$ that follows from the comparison of the differential $\partial_x i$ with the self-field term $\sim -(d/2\pi\lambda^2)i(x)\ln[(W/2-x)/(W/2+x)]$ on the right-hand side. Estimating the self-field (3) from the current in the absence of screening, see Eqs. (4) and (5) below, we find that $B_{\rm self} \sim -(W/\lambda_\perp)H$. For 2D superconducting strips with $W \ll \lambda_\perp$, the self-field is negligible and the total magnetic field inside and outside the material has the same value $B \approx H$. The equation for the current distribution inside such 2D superconducting thin films therefore simplifies to

$$\frac{d\,i}{d\,x} \approx -\frac{cd}{4\pi\lambda^2}[H - n(x)\Phi_0], \tag{4}$$

a simple first-order differential equation with a source term that depends on the vortex density $n(x)$.

In the following, we will integrate Eq. (4) to find the current density profile at given field H and fixed bias current $I = \int i(x)\,dx$ as summarized in Figs. 3(b)–3(e), and 4(b). In doing so, we will determine the critical current $I_c(H)$ as shown in Fig. 2 and characterize the (hysteretic) critical state of thin superconductors with $d \ll \lambda$.

A. Without bias current $I = 0$

To start with, we consider Eq. (4) in the absence of external bias currents, $I = 0$. In the Meissner state, i.e., when $n(x) = 0$, the current density profile is linear,

$$i(x) = -\frac{c\,dH}{4\pi\lambda^2}x, \tag{5}$$

and takes opposite values on the two sides of the 2D film.

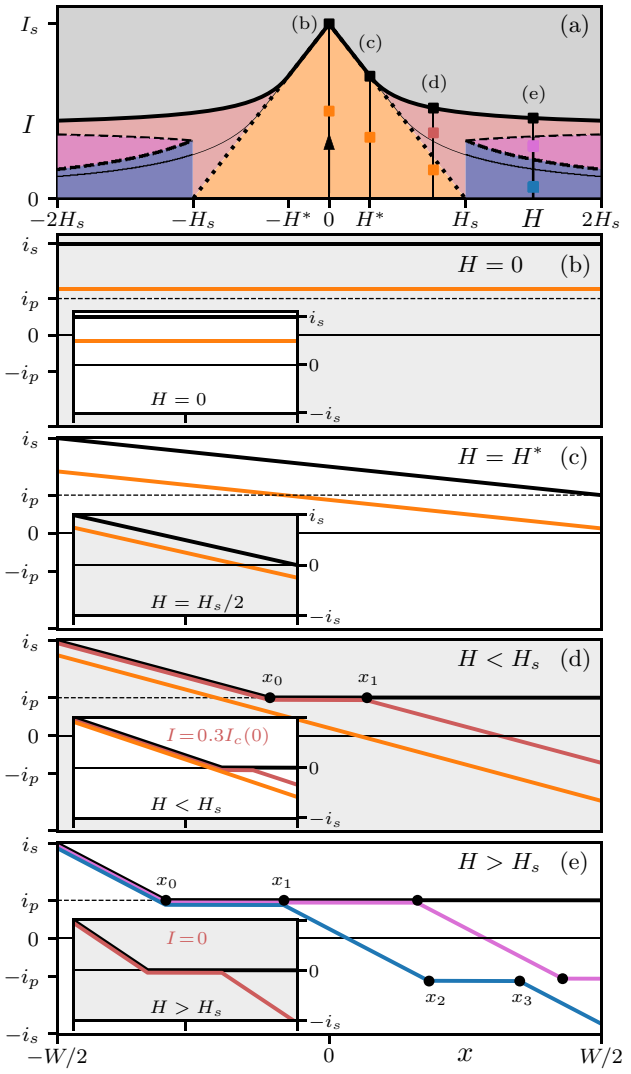

FIG. 3. Current density profiles at different combinations of H and I (for a film initially prepared with $I = 0$) corresponding to the colored squares in the hysteretic diagram (a), cf. Fig. 2. (b) At zero field, $i(x) = I/W$ (solid-orange line) everywhere and no vortex enters the sample until $I = I_c(0)$ (solid-black line). (c) For $H \leqslant H^*$, the superconductor remains in the Meissner state (solid-orange line) until $I = I_c(H)$ (solid-black line) is reached. At $H = H^*$, $i(x)$ reaches i_s (i_p) on the left (right) edge; vortices penetrating the sample at $-W/2$ stop just before exiting at $+W/2$. (d) For larger fields $H^* < H < H_s$, the state of the superconductor depends on the value of the bias current I. At small $I < I_s(H)$ (orange), the sample is in the Meissner state. For larger currents $I > I_s(H)$ (red), vortices penetrate from the left and form a box with $i(x) = i_p$ for $x \in [x_0, x_1]$ (solid-black dots). At the critical current $I = I_c(H)$ (black), x_1 reaches $W/2$ and vortices start flowing across the sample upon further increase of I. (e) For fields $H \geqslant H_s$, the superconductor is always in the mixed state. Two symmetric vortex boxes are present at $I = 0$. For $I \leqslant I_t(H)$ (blue), the right of the two vortex boxes conserves the vortex number attained at $I = 0$. At larger currents, vortices start leaving the right box (magenta), until this disappears when $I = I_d(H)$; only one vortex box remains at currents $I > I_d(H)$ (red). The currents I_t and $I_d > I_t$ are shown with black-dashed lines in (a). The insets show the current distribution for the same field values for the case of vanishing bulk pinning, i.e., $i_p = 0$ (where $H^* = H_s/2$). The black and orange lines refer to transport currents $I = I_c$ and $I = I_c/2$ at $i_p = 0$, respectively.

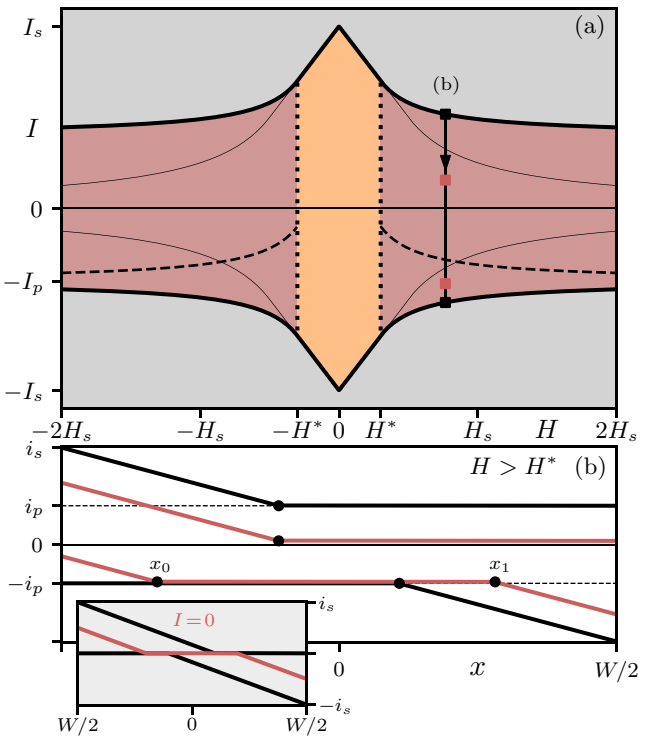

FIG. 4. Current density profile at different combinations of H and I [for a film prepared with $I = I_c(H)$] corresponding to the colored squares in the hysteretic diagram (a), cf. Fig. 2. The superconductor remains in the Meissner state (orange) for small fields $|H| \leqslant H^*$. For larger fields $|H| > H^*$ the film *always* resides in the mixed state with one vortex box (red), different from the situation with increasing currents from zero discussed in Fig. 3. (b) At $I = I_c(H)$ (upper black line) the vortex box extends to the right edge of the sample and $i(x > x_0) = i_p$. Decreasing the current (upper-red line), vortices stay trapped, the box remains in place (upper red line), and the current density profile $i(x)$ rigidly shifts downwards. When $I = I_c(H) - 2I_p < 0$ [black-dashed line in (a)], the plateau in $i(x)$ reaches $-i_p$; upon further decrease of I, the vortex box shifts to the left conserving its size (lower-red line). At $I = -I_c(H)$ (lower-black line), the current density profile $i(x)$ touches $-i_s$ at the right edge $W/2$ and the vortex box has reached the left edge, resulting in an overall inversion $i(x) \to -i(-x)$ when going from $I_c(H)$ to $-I_c(H)$. The inset shows the evolution of the current density profile with decreasing current in the absence of bulk pinning.

Upon increasing the magnetic field H, so-called Pearl vortices start penetrating the superconductor; the latter are disk-like objects with supercurrents circulating on the scale $\lambda_\perp$ that produce a magnetic field of monopolar shape in the upper/lower half-plane, in contrast to the usual flux-tube associated with the Abrikosov vortex in a bulk sample. The nucleation of vortices from the edges of the superconducting film is hampered by the presence of a steep surface barrier. In the ideal scenario, the latter can be overcome by a transport- or field-induced current density j when this approaches the depairing current density j_0 at the boundary. Indeed, in the narrow 2D film ($W \ll \lambda_\perp$) the self-field can be neglected and the current distribution (at zero field) is homogeneous and equivalent to that in a 1D wire [52], which results in the criterion $j_s = j_0$ for the critical surface current density j_s. In real materials, the critical current density j_s where vortices start penetrating inside the superconductor is typically smaller than the depairing value [53] due to edge roughness, imperfections, or voltage gating [25].

In the absence of an external bias current $I = 0$, vortices penetrate inside the sample when the magnetic field reaches the surface penetration value H_s, i.e., when the magnitude of the current density $i(x)$ at the edges $x = \pm W/2$ reaches the critical value $i_s \equiv j_s d$. Using Eq. (5), the condition $i_s = [(cd\,H_s)/(4\pi\lambda^2)](W/2)$ provides us with the surface penetration field

$$H_s \equiv \frac{8\pi}{c\,d}\frac{\lambda^2}{W}\,i_s \tag{6}$$

where the superconductor enters the mixed state for $I = 0$. Using the above criterion $j_s = j_0$ for the surface current density, the vortex penetration field (6) reads

$$H_s = \frac{2\Phi_0}{3\sqrt{3}\pi\xi W} \sim \frac{\Phi_0}{\xi W} \sim \frac{\lambda}{W}H_c, \tag{7}$$

where the last estimate relates H_s to the thermodynamic critical field $H_c \equiv \Phi_0/2\sqrt{2}\pi\lambda\xi$ that sets the magnetic scale for the penetration of vortices across the surface of a bulk sample in a parallel field [4] (in Ref. [49], another criterion was used that resulted in a smaller penetration field $H_s = \Phi_0/2\pi\xi W$, see also Refs. [47,48] where the same criterion gives $H_s = \Phi_0/2\pi\xi d$ for a film in parallel field).

In the absence of bulk pinning, the vortices that penetrate inside the 2D film accumulate in a finite region around the center of the superconductor where $i(x) = 0$. In this region, the derivative di/dx in Eq. (4) vanishes, implying that the density is constant and given by $n = H/\Phi_0$; this "vortex box" replaces the "vortex dome" in the flat sample. The solution of (4) then consists of piecewise linear parts $i(x) = \mp[i_s - (cd\,H/4\pi\lambda^2)(W/2 \mp x)]$ near the vortex-free right and left edges, respectively, and a vanishing current $i(x) = 0$ in the vortex box; the two solutions merge at the box edges $\pm x_v(H)$ that derive from the condition $i(\pm x_v) = 0$ imposed on the linear part of the solution,

$$x_v(|H| > H_s) = \frac{W}{2}\left(1 - \frac{H_s}{|H|}\right). \tag{8}$$

The resulting current density profile is shown as a red line in the inset of Fig. 3(e) further below.

At finite bulk pinning $j_p > 0$ and large enough fields $|H| > H_s$, vortices from both sides are driven towards the center of the film as long as the local current density $i(x)$ stays larger than i_p. Hence, two symmetric vortex plateaus $|x| \in [x_i(H), x_o(H)]$ appear away from the boundaries, see Fig. 1(c) in the Introduction. The current density is constant and equal to i_p inside these regions and thus the slope di/dx in (4) vanishes, again producing the vortex density $n(x) = H/\Phi_0$. Matching the constant current $i = i_p$ within the plateaus to the (properly shifted) linear current densities (5) in the vortex-free regions, we find the expressions for the inner and outer boundaries $x_i(H)$ and $x_o(H)$,

$$(x_i, x_o)(|H| > H_s) = \frac{W}{2}\left(\frac{H_p}{|H|},\ 1 - \frac{H_s - H_p}{|H|}\right), \tag{9}$$

with

$$H_p \equiv \frac{8\pi}{c\,d}\frac{\lambda^2}{W}\,i_p \tag{10}$$

the field where the Meissner screening currents (5) reach $\pm i_p$ at the edges of the superconductor. The above results will also be relevant in the calculation of the magnetic moment $m(H)$ in Sec. IV below, where the hysteretic behavior at decreasing H after a field reversal at H_0 will be considered as well.

B. Critical bias current $I = I_c(H)$

We move on to study the critical state preceding the onset of dissipation, i.e., when a critical current $I = I_c(H)$ is applied to the superconductor. While the $I = 0$—finite H scenario is relevant to magnetization experiments, the critical state with $I = I_c(H)$ is of great importance for transport experiments.

In the presence of a finite and homogeneous across x transport current $I = \int dx\, i(x)$ fed to the sample, the solution of the Maxwell-London equation (4) in the Meissner state picks up an additional term I/W,

$$i(x) \approx \frac{I}{W} - \frac{cd\,H}{4\pi\lambda^2}x, \tag{11}$$

see Figs. 3(b) and 3(c) where the flat and tilted current distributions at vanishing and finite fields are shown. Note that the linear term $\propto -Hx$ induced by the external field H does not contribute to the transport current.

Criticality is reached when the magnitude of the current density $i(x)$ at either (or both) edges $x = \pm W/2$ reaches the surface critical current i_s, at which point vortices start penetrating the film. Using Eq. (11), we find the critical current at vanishing magnetic field

$$I_c(0) = I_s \equiv i_s W \tag{12}$$

with vortices/antivortices entering from the two edges. At positive (negative) fields and positive current bias $I > 0$, the screening term in Eq. (11) favors the nucleation of vortices from the left (right) edge of the superconductor when $i(\pm W/2) = I_c/W \mp (cd\,H/4\pi\lambda^2)W/2 = i_s$, and the critical current reads [49,50] [we make repeated use of Eqs. (6) and (10) to express $cdW^2/8\pi\lambda^2$ through i_s/H_s or i_p/H_p]

$$I_c(H) = I_s\left(1 - \frac{|H|}{H_s}\right). \tag{13}$$

Equation (13) defines the critical current in the Meissner state; its linear cusp at the origin is the hallmark of surface pinning and corresponds to the linear portions of the black solid line in Fig. 2. The result is valid as long as the current density $i(x)$ is larger than depinning everywhere, $i(x) > i_p$, allowing vortices to traverse the superconductor without stopping.

The field $H \equiv H^* > 0$ where $i(x)$ first touches i_p then defines a new regime where vortices that enter from the left edge stop because of bulk pinning just before exiting at the right edge. This brings the superconductor to the onset of the mixed state, with the corresponding critical state shown by the solid-black line in Fig. 3(c). Imposing the conditions $i(-W/2) = i_s$ and $i(W/2) = i_p$ valid at $H = H^*$ on Eq. (11), we obtain the relation $i_s - i_p = (cd\,H^*/4\pi\lambda^2)(W/2)$ that sets the transition between Meissner and mixed critical states at,

$$H^* \equiv \frac{H_s - H_p}{2}. \tag{14}$$

Increasing the field beyond H^*, the critical current density profile $i(x)$ turns steeper on the left and the mixed state region expands from the right edge into the film, see the black-solid lines in Figs. 3(d) and 3(e). Currents $i_p \leqslant i \leqslant i_s$ in the linear region push the vortices into the superconductor until they stop and accumulate to form a vortex box with constant density $n(x) = H/\Phi_0$ within the region $[x_0(H), W/2]$. The Maxwell-London equation (4) then tells that the current density $i(x)$ is constant within the vortex box, assuming the value $i(x) = i_p$ at criticality. Matching the linear and constant portions of $i(x)$, we find the result [see also Appendix A and Eq. (9)]

$$x_0(H) = -\frac{W}{2}\left(1 - \frac{2H^*}{H}\right). \tag{15}$$

Integrating the resulting current profile $i(x)$, we find the critical current curve $I_c(H)$ in the form [we define $I_p = i_p W$ and repeat the low-field result Eq. (13); the extension to negative fields $H < -H^*$ is trivial]

$$I_c(|H| < H^*) = I_s\left(1 - \frac{|H|}{H_s}\right), \tag{16}$$

$$I_c(|H| > H^*) = I_p\left(1 + \frac{(H^*)^2}{|H|H_p}\right). \tag{17}$$

The presence of the finite vortex box at fields $|H| > H^*$ contributes with the current $i_p[W/2 - x_0(H)]$ to $I_c(H)$ that results in the nonlinear dependence of the critical current I_c on the field H. In the limit of large magnetic fields $H \gg H^*$, $x_0 \to -W/2$ and $I_c(H)$ saturates to $i_p W = I_p$.

In the absence of bulk pinning, $i_p = 0$, the result (17) reduces to $I_c(|H| > H_s/2) = I_s\,(H_s/4H)$ and the critical current drops towards zero at large fields, see Refs. [49,50]. This result, combined with the cusp of Eq. (16), is of quite general nature and applies to flat samples with surface or geometrical barrier and $x \leftrightarrow -x$ symmetry [54]. The cusp for $|H| < H_s/2$ describing the *linear* Meissner regime can be obtained with the help of the following consideration: Linearity tells us that the current density profile $i(x)$ must have the form $i(x) = I f_I(x) + H f_H(x)$, with $f_{I,H}(x)$ two (symmetric and antisymmetric in x) shape functions. The conditions for maximal current at zero field H, $i(\pm W/2) = i_s$, and maximal field H_s at vanishing current I, $i(-W/2) = -i_s$, relate $I_s = i_s/f_I(\pm W/2)$ and $H_s = \pm i_s/f_H(\pm W/2)$, from which follows the result (16). The linear form is valid until first penetration of vortices; the corresponding conditions $i(W/2) = i_s$ and $i(-W/2) = 0$ (valid in the absence of pinning) determine the penetration field $H^* = H_s/2$.

In the opposite limit of strong bulk pinning $i_p \to i_s$, the linear peak Eq. (16) at small fields, that is due to surface pinning, gets absorbed into the flat background due to bulk pinning. The results (16) and (17) compactly illustrate the relevance of surface and bulk pinning: The surface barrier dominates the low-field regime at $|H| < H^*$ and produces a linear cusp in $I_c(H)$, while bulk pinning shapes the large-field region $|H| > H^*$ and produces a saturation in the tails.

When comparing the above theoretical results for $I_c(H)$ to experiments, we note that the magnitude of $I_c(H)$ depends, via I_s, on the value i_s of the critical current density at the edges. The latter can vary from sample to sample due to edge imperfections, rendering the task of predicting the value of the critical current not straightforward. This is not the case, however, for the slope dI_c/dH in the Meissner state: taking the derivative of (13), we find that

$$\frac{dI_c(H)}{dH} \approx -\frac{c}{8\pi}\frac{d}{\lambda}\frac{W^2}{\lambda^2} \tag{18}$$

is independent of i_s. The slope of $I_c(H)$ thus assumes a universal value, determined only by the London length λ and the width W of the film.

C. Finite bias current $0 < I < I_c(H)$

We proceed with the study of the critical state for arbitrary bias current I at fixed field H. At small fields $|H| < H^*$, the film always resides in the Meissner phase and thus behaves reversibly, with $n(x) = 0$ and $i(x)$ given by the shifted linear profile (11). At larger fields $|H| > H^*$, the presence of vortices gives rise to hysteretic behavior: We will first study the vortex and current density profiles $n(x)$ and $i(x)$ for increasing currents I at fixed H in samples initially prepared at zero bias current $I = 0$ and focus on currents decreasing from $I_c(H)$ in a second step. Without loss of generality, we will consider positive magnetic fields H, such that vortices shift towards the right of the superconductor when $I > 0$. To benefit the reader, we will defer the detailed derivations and expressions for the edges of the vortex boxes to Appendix A.

1. *Increasing the current from $I = 0$*

In the absence of bias currents and for fields $|H| \leqslant H_s$, the superconductor is in the Meissner state. Upon increasing I, vortices first penetrate inside the sample when the current density (11) reaches i_s at either of the two edges, cf. the derivation of (13), i.e., along the line

$$I_s(H) = I_s\left(1 - \frac{|H|}{H_s}\right), \quad \text{for} \quad |H| < H_s. \tag{19}$$

This (black-dotted) line in Fig. 3(a) separates the Meissner from the mixed states when starting from $I = 0$ with $|H| < H_s$ and coincides with the critical current (13) at low fields $|H| \leqslant H^*$. As a result, for increasing bias currents I, the Meissner state encompasses the orange region in Fig. 3(a).

For larger bias currents $I > I_s(H)$, vortices accumulate inside the superconductor, forming a vortex box that extends between $x_0(H)$ and $x_1(H, I)$; the box boundaries $x_0(H)$ and $x_1(H, I)$ are again obtained by matching the linear and constant ($i = i_p$) portions of the current profile derived from the Maxwell-London equation (4) and fixing the current $I = \int dx\, i(x)$, see Appendix A 1. The solution $x_0(H)$ is still given by Eq. (15), while $x_1(H, I)$ depends additionally on the current I and reads

$$x_1(H, I > I_s) = W\left[\frac{1}{2} - \sqrt{\frac{H_p}{H}\frac{I_c(H) - I}{I_p}}\right]. \tag{20}$$

The current density profile for a situation away from $I_s(H)$ is shown in red in Fig. 3(d); the current distribution evolves into the critical one (black lines) as the bias current is increased to $I_c(H)$ and the vortex box touches the right edge of the sample, allowing vortices to leave the superconductor.

For fields $|H| \geqslant H_s$, the superconductor is in the mixed state already for vanishing bias currents $I = 0$, with two symmetric vortex boxes $[x_0 = -x_o, x_1 = -x_i]$ and $[x_2 = x_i, x_3 = x_o]$ present inside the sample. Upon increasing the bias current, the left box $[x_0, x_1]$ expands, as new vortices enter the superconductor from the left edge, while the right box $[x_2, x_3]$ shifts towards the right edge and conserves its size, as vortices therein are trapped by the surface currents and cannot leave the film. Again, the boundaries of the vortex boxes are found by imposing that $i(x)$ (made up from linear and constant portions) is continuous across the superconductor and that $I = \int dx\, i(x)$; the corresponding expressions are given by Eqs. (A11)–(A13), and (A2) of Appendix A 1 and a typical current density profile is shown in blue in Fig. 3(e).

When the bias currents reaches

$$I_t(H) \equiv I_s\frac{(H^*)^2 + 2H^*H_p}{H_s|H|}, \tag{21}$$

the boundary x_3 of the right vortex box touches $W/2$ and the box starts shrinking as the vortices gradually leave the superconductor. The current density profile typical for this regime is shown in magenta in Fig. 3(e) and the corresponding expressions for x_2, x_1 and x_0 are given by Eqs. (A16) and (A17) as well as (A2). When $x_2(I, H) = W/2$, the right vortex box has disappeared completely and only the left box remains; this happens when the bias current reaches

$$I_d(H) \equiv I_p\frac{(H^*)^2 + |H|H_p - H_p^2}{H_p|H|}. \tag{22}$$

Equations (21) and (22) correspond, respectively, to the lower and upper black-dashed curves in the diagram Fig. 3(a). The two curves cross at H_s, where (i) the right box touches the sample edge at $W/2$ and (ii) its width vanishes. For bias currents $I > I_d(H)$, the current density profile displays a single plateau, i.e., there is only one surviving vortex box whose boundaries x_0 and x_1 are described by the same expressions (15) and (20) as obtained for fields $|H| \leqslant H_s$; finally, the critical current $I_c(H)$ is reached when $x_1 = W/2$.

2. *Decreasing the current from $I = I_c(H)$*

We decrease the transport current I from the critical value $I_c(H)$ at fixed field H in order to study the hysteretic effects in current I (hysteretic effects in H will be studied in Sec. IV below). In preparing the sample, we wish to avoid complications associated with the dissipative state [e.g., a potential strong rearrangement in the current profile $i(x)$] and therefore drive the film close to, but below $I_c(H)$ before decreasing the current I.

Starting with small fields $|H| < H^*$, the film always remains in the Meissner state and hence behaves reversibly. Going to higher fields $|H| > H^*$ and preparing the film at $I = I_c(H)$, vortices have populated the superconductor such that the sample remains in the mixed state for all values of the bias current $I < I_c(H)$, see the red region in Fig. 4(a). Decreasing

the current I below $I_c(H)$ the vortices that are trapped inside the superconductor remain trapped in the region $[x_0, W/2]$, with x_0 given by Eq. (15), see the upper solid-black curve in Fig. 4(b), and the local density of vortices $n(x)$ does not change as long as $|i(x)|$ remains below its bulk critical value i_p. As a result, the current density profile $i(x)$ is rigidly shifted downwards, see the upper solid-red line in Fig. 4(b), until the current in the plateau first reaches $-i_p$ at $I = I_c(H) - 2I_p < 0$ [black-dashed line in (a)]. At this current, the vortices start shifting to the left and a new vortex-free region with $di/dx \propto -H$ forms close to the right edge of the superconductor [lower solid red curve in (b)]; the position $[x_0(H, I), x_1(H, I)]$ of the vortex box in the region $I_c - 2I_p > I > -I_c$ is given by Eqs. (A19) and (A20) in Appendix A 2. Finally, when I is further decreased to $-I_c(H)$, the current density reaches $-i_s$ at the right boundary $W/2$ in the same instant that x_0 touches the left boundary $-W/2$, thus realizing the critical state appertaining to $-I_c(H)$. Hence, in the process of reducing the current I from $I_c(H)$ to $-I_c(H)$, the vortex box has kept its size and has shifted from the right side to the left side of the film. Also, note that decreasing the current from critical, the vortex configuration in the mixed state always contains a single vortex box, see Fig. 4(a), different from the behavior with increasing currents where the number of vortex boxes changes between two and one, see Fig. 3(a).

III. SUPERCONDUCTING DIODE EFFECT IN ASYMMETRIC 2D THIN FILMS

Superconducting films have a long tradition in technological applications, including Josephson junction-based devices in electronics and many types of sensors, e.g., for magnetic fields (SQUIDS) or photodetectors (bolometers). Another application that has been much discussed recently is the superconducting diode effect (SDE) [26–33,35–43] in 2D superconductors. In this type of inductive device, an ac current drive is applied to produce a dc voltage, the opposite of the usual capacitive setup in a semiconductor where an ac voltage drive produces a dc current. A simple mechanism producing this effect is provided by the asymmetric vortex motion within a superconducting film upon current reversal that produces a nonreciprocal transport characteristic. Such a vortex-based SDE can be realized through asymmetric surface barriers generating different surface critical current densities $i_{s,L}$ and $i_{s,R}$ at the left and right edges of the film, respectively. This kind of asymmetry is ubiquitous in real thin films and can result from device imperfections [50] or deliberate design [40]. Another vortex-based source of nonreciprocal transport is the ratchet effect in bulk vortex pinning producing different depinning currents $i_{p,L}$ and $i_{p,R}$ for vortices incident from the left and right side, respectively. Such a bulk asymmetry does not naturally occur in thin-film devices, but can be realized in nanostructured devices [29,55–58] and twisted moiré superconductors [26], where the degree of asymmetry can directly be controlled by means of an applied gate voltage. While the surface barrier asymmetry manifests in the low field peak of $I_c(H)$, the asymmetry in bulk pinning shows up in the tails of $I_c(H)$ at large fields.

Alternative mechanisms [43] involving symmetry breaking on a microscopic level have been discussed in order to generate a superconducting diode effect. Prominent examples are noncentrosymmetric materials [59–61], finite momentum pairing [62], or chiral superconductors [63]. At the same time, use of the SDE has been proposed as a means to infer spontaneous symmetry breaking in exotic superconductors [63]. However, care has to be taken in order not to confuse an intrinsic mechanism with the simple vortex-based origin where time-reversal and inversion symmetries are broken on a macroscopic level, see Ref. [64] and the discussion in Sec. III C below.

In the present section, we provide a simple and quantitative analysis of the superconducting diode effect in terms of our critical state model, including also the effect of bulk pinning. In Sec. III A below, we will first determine the nonreciprocal critical currents $I_c^+(H)$ and $I_c^-(H)$ for different drives along and opposite to the y axis. Subsequently, we will find quantitative results for the diode efficiency, see Sec. III B, and then compare our findings with recent experiments, Sec. III C.

A. Critical current in asymmetric 2D thin films

We choose a film asymmetry where the surface critical current density $i_{s,L}$ and surface penetration field $H_{s,L} = (8\pi\lambda^2 i_{s,L}/cdW)$, see (6), at the left edge are larger than their counterparts $i_{s,R}$ and $H_{s,R}$ at the right edge. Moreover, for the main part of this section, we will assume that the surface critical current densities are larger than either depinning current, i.e., $i_{s,(R,L)} > i_{p,(R,L)}$.

For such an asymmetric setup, criticality at zero field $H = 0$ is realized when the homogeneous current density $i(x)$ in (11) reaches the smaller critical value $i_{s,R}$ at the right boundary $x = W/2$, hence, $I_c(0) = i_{s,R}W$, see the blue line in the inset of Fig. 5. Vortices then enter the sample from the right side only. Since the application of a field $H > 0$ tilts the current profile, the current I can be further increased until reaching the critical surface current $i_{s,L}$ at the left film boundary, i.e., $i(-W/2) = i_{s,L}$, at a finite field $H_{\max} > 0$, see the orange line in the inset of Fig. 5. Using Eq. (11), the two conditions $i(-W/2) = i_{s,L}$ and $i(W/2) = i_{s,R}$ transform to the relations

$$i_{s,R}W = I_c(0) = I_c(H_{\max}) - \frac{cdW^2}{8\pi\lambda^2}H_{\max}, \tag{23}$$

$$i_{s,L}W = I_c(H_{\max}) + \frac{cdW^2}{8\pi\lambda^2}H_{\max}. \tag{24}$$

The first equation relates the peak field $H_{\max}$ to the macroscopic difference in the total currents $I_c(H_{\max}) - I_c(0)$,

$$H_{\max} = \frac{8\pi\lambda^2}{cdW}[I_c(H_{\max}) - I_c(0)], \tag{25}$$

while the sum and differences of the equations (23) and (24) express the macroscopic quantities $I_c(H_{\max})$ and $H_{\max}$ through the surface parameters $i_{s,(R,L)}$ and $H_{s,(R,L)}$,

$$I_c(H_{\max}) = (I_{s,L} + I_{s,R})/2, \tag{26}$$

$$H_{\max} = (H_{s,L} - H_{s,R})/2. \tag{27}$$

In a next step, we account for the presence of bulk pinning by repeating the strategy adopted for the symmetric film and compute $I_c(H)$. Defining $H_R^* \equiv (H_{s,R} - H_{p,R})/2$ and $H_L^* \equiv (H_{s,L} - H_{p,L})/2$ as the right and left generalizations of

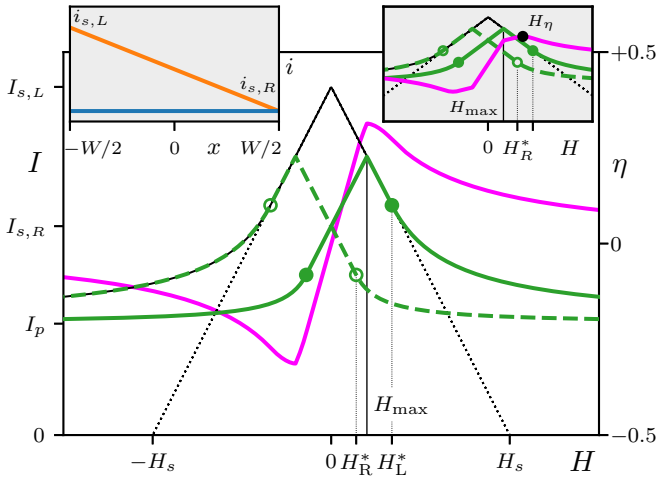

FIG. 5. Critical current $I_c(H)$ as a function of magnetic field H for a symmetric (black line) and an asymmetric system (green). The critical currents $I^+(H)$ for a positive current directed along y (solid green) and the one for a negative current $I_c^-(H) = -I_c^+(-H)$ directed along $-y$ are no longer the same (the dashed-green line shows the modulus $|I_c^-(H)|$). The solid (empty) dots indicate the positive (negative) critical currents at the fields $\mp H_R^*$ and $\pm H_L^*$. The finite-peak fields $\pm H_{\max}$ produce the nonreciprocal transport properties characteristic for a superconducting diode; its efficiency (magenta line) is quantified by the parameter η defined in Eq. (29). For the present choice of parameters (see text), the diode efficiency peaks at $H_{\max}$. (Top left inset) Current density profile $i(x)$ at criticality in the asymmetric sample for $H = 0$ (blue line) and $H = H_{\max}$ (orange line). (Top right inset) Situation for $H_{\max} < H_R^*$ where η exhibits a maximum at H_η to the right of $H_{\max}$.

the H^* field in Eq. (14), we find that

$$I_c(H) \approx \frac{c}{8\pi}\frac{d}{\lambda}\frac{W^2}{\lambda^2}\begin{cases} H_{p,R} + (H_R^*)^2/|H| & \text{for } H \leqslant -H_R^*, \\ H_{s,R} + H & \text{for } -H_R^* \leqslant H \leqslant H_{\max}, \\ H_{s,L} - H & \text{for } H_{\max} \leqslant H \leqslant H_L^*, \\ H_{p,L} + (H_L^*)^2/H & \text{for } H \geqslant H_L^*. \end{cases} \tag{28}$$

Figure 5 shows the comparison of the overall field dependence of the critical current $I_c(H)$ for a symmetric film (black line, $i_p = 2i_s/5$) and an asymmetric sample with $(i_{s,L} - i_{s,R})/(i_{s,L} + i_{s,R}) = 1/4$ and symmetric bulk pinning (green line, $i_{s,L} = i_s$, $i_{s,R} = 3i_s/5$, $i_{p,L} = i_{p,R} = i_p = 2i_{s,L}/5$). With these parameters, the critical current $I_c(H)$ attains its maximum at $H_{\max} = (H_{s,L} - H_{s,R})/2 = H_{s,L}/5$ with $H_L^* = 3H_{s,L}/10$ and $-H_R^*$ delimiting the linear segments of $I_c(H)$, $H_R^* = H_{s,L}/10 < H_{\max}$. For a current flow in the opposite direction, the left and right surfaces are exchanged and the solid-green line in Fig. 5 is reflected with respect to the origin, with the peak field $H_{\max}$ changing sign. Defining $I_c^+(H) = I_c(H)$ and $I_c^-(H)$ as the critical currents flowing in the positive and negative directions, respectively, we find them related through $I_c^+(H) = -I_c^-(-H)$, as required by time reversal symmetry. The absolute value $|I_c^-(H)|$, the dashed-green line in Fig. 5, is thus a mirror copy of $I_c^+(-H)$ reflected with respect to the $H = 0$ axis. Asymmetric bulk pinning with $i_{p,R} \neq i_{p,L}$ results in different asymptotic currents $I_c(H \gg H_L^*) \to i_{p,L}W$ and $I_c(H \ll -H_R^*) \to i_{p,R}W$. Hence, while surface asymmetry manifests in the shift of the peak at small fields, an asymmetry in bulk pinning manifests in the tails at large fields.

B. Efficiency of superconducting diode

Given the difference in the positive and negative critical currents, asymmetric 2D superconducting films display nonreciprocal transport properties that can be exploited in the fabrication of a superconducting diode [27]. The nonreciprocal character of these devices is commonly quantified by the (antisymmetric) diode efficiency

$$\eta(H) \equiv \frac{I_c^+(H) - |I_c^-(H)|}{I_c^+(H) + |I_c^-(H)|} = \frac{I_c(H) - I_c(-H)}{I_c(H) + I_c(-H)} \tag{29}$$

shown as the magenta line in Fig. 5; in Eq. (29), we have used that $I_c(H) = I_c^+(H) = -I_c^-(-H)$ and $I_c(H)$ is given by Eq. (28). As the system obeys time-reversal symmetry, the diode efficiency vanishes for $H = 0$. Moreover, it saturates to the constant value

$$\eta(H \gg H_L^*) \approx \frac{H_{p,L} - H_{p,R}}{H_{p,L} + H_{p,R}} \tag{30}$$

at large fields where the asymmetric bulk pinning dominates over the effects of surface barriers and reduces to zero for symmetric bulk pinning $H_{p,R} = H_{p,L}$, see Fig. 5. The sign of η indicates the polarity of the diode-like behavior.

The full field dependence $\eta(H)$ is straightforwardly obtained by inserting the expression (28) for the critical current $I_c(H)$ into the definition (29) of η, see the magenta line in Fig. 5. Below, we focus on the position of the maximum $\eta_{\max}$ in the efficiency $\eta(H)$ for the case of symmetric bulk pinning $H_{p,L} = H_{p,R} = H_p$. We start by analyzing the situation at small asymmetry where $H_{\max} < H_R^*$, shown in the top-right inset of Fig. 5. In this situation, the cusp of $I_c(H)$ at $H_{\max}$ resides within the linear segment of $|I_c^-(H)| = I_c(-H)$ that extends up to H_R^*. Similarly, $I_c^+(H) = I_c(H)$ drops linearly up to H_L^*. As a result, the numerator $I_c(H) - I_c(-H)$ in Eq. (29) stays constant in the interval $[H_{\max}, H_R^*]$ while the denominator decreases, hence, $\eta(H)$ rises with increasing $H > H_{\max}$. With a continuous derivative of $I_c^\pm$ across H_R^*, the efficiency grows further and reaches its maximum at a field $H_\eta > H_R^*$ where $\partial_H \eta(H_\eta) = 0$, resulting in

$$H_\eta = H_R^*\left(\sqrt{\left(\frac{H_R^*}{H_p}\right)^2 + \frac{H_{s,L}}{H_p}} - \frac{H_R^*}{H_p}\right) > H_R^*. \tag{31}$$

The maximal diode efficiency is then found by evaluating the expression (29) for η at this field,

$$\eta_{\max} = \frac{\left(H_{s,L}^2 - H_p^2\right)/(H_R^*)^2 - 4\sqrt{1 + H_p H_{s,L}/(H_R^*)^2}}{(H_p + H_{s,L})^2/(H_R^*)^2 + 4}. \tag{32}$$

When $H_{\max}$ grows larger, the nonanalyticity in $I_c(H)$ at $H_{\max}$ approaches H_η and the above derivation breaks down at $H_{\max} = H_\eta$. For $H_{\max} > H_\eta$, the peak in $I_c(H)$ pins the maximum of η and hence $\eta_{\max}$ is achieved exactly at $H_{\max}$; we then enter the domain of large asymmetry (shown in the main part

of Fig. 5) where

$$\eta_{\max} = \eta(H_{\max}) = \frac{H_{s,L} - H_{\max} - H_p - (H_R^*)^2/H_{\max}}{H_{s,L} - H_{\max} + H_p + (H_R^*)^2/H_{\max}}. \quad (33)$$

Let us consider how much the diode efficiency can be increased in a strongly asymmetric device (but with symmetric bulk pinning $H_{p,L} = H_{p,R} = H_p$) by decreasing the strength of the weaker (in our convention, the right) surface barrier $H_{s,R}$ until eventually reaching $H_p = H_{s,R}$. When this happens, the right edge does no longer play any role as nucleated vortices are stuck until they can overcome vortex pinning in the bulk. The maximal possible diode efficiency is therefore obtained by replacing the right surface barrier with the bulk pinning parameter, i.e., by substituting $H_{s,R} = H_p$ in Eq. (33), yielding

$$\max[\eta_{\max}] = \eta(H_{\max})\Big|_{H_{s,R}=H_p} = \frac{H_{s,L} - H_p}{H_{s,L} + 3H_p} \quad (34)$$

as the maximal possible η in a device with finite (symmetric) bulk pinning.

C. Comparison with experiments

The superconducting diode can be engineered in 2D thin films with asymmetric surface barriers as proposed and studied in Ref. [27]. This type of inductive diode has recently been realized in conventional films (such as niobium and vanadium) and its functionality has been understood [40]. Here, we will analyze and discuss two recent experimental studies [32,40]; in both of these studies, the data for the critical current $I_c(H)$ look very similar, but the conclusions drawn by the authors turn out very different. In a first step, we compare the results of our 2D critical state model with their experimental data on the critical current $I_c(H)$ and subsequently discuss the observed efficiency η in the light of our findings above. The latter has been used to conjecture [32] that the diode effect is not vortex based, as the maximum in η was found at a field beyond $H_{\max}$; as demonstrated above, this finding is nevertheless consistent with our 2D critical-state-based vortex model.

We begin with the analysis of $I_c(H)$ as depicted in Fig. 1 of Ref. [32]; the observed $I_c(H)$ curve shows the typical shape expected for a surface dominated sample with a sharp cusp at small fields that compares well with our results in Fig. 5. The experiment was performed in a $NbSe_2$ double layer (thickness $d \approx 1.5$ nm and width $W \approx 250$ nm of the constriction) and clear signatures of nonreciprocal transport and a superconducting diode effect was observed. Transforming the maximal critical current $I_c(H_{\max})$ to a current density j_c, we find a value $j_c \approx 3 \times 10^6$ A/cm^2. This has to be compared with the depairing current density j_0 that can be obtained from phenomenological parameters ξ and λ for $NbSe_2$; while the bulk value for $\xi \approx 10$ nm seems to provide a good estimate (as T_c and H_{c2} in the film are similar to the bulk [26]), the bulk value $\lambda \approx 250$ nm may have to be corrected for the film. Taking nevertheless these values, we find a value $j_0 \approx 1.6 \times 10^7$ A/cm^2; a reduction $j_s < j_0$, here by a factor 5, is expected due to surface imperfections and we consider the agreement quite satisfactory, also with view to our uncertainty in the size of λ.

Next, we evaluate the slope $\partial_H I_c(H)$ near the current peak and find a value $\partial_H I_c(H) \approx 10^{-4}$ A/T. This has to be compared with the prediction in Eq. (18) that includes the parameters $\lambda_\perp = 2\lambda^2/d$ and W. Using the above parameters for d and λ, we find that $\lambda_\perp \approx 80$ μm that results in a small parameter $W/\lambda_\perp \approx 3 \times 10^{-3}$, quite small indeed. On the other hand, we can extract W by comparing the experimental result for the slope $\partial_H I_c(H)$ with the prediction in Eq. (18) and find the value $W \approx 100$ nm, an outcome that is smaller but still acceptable in comparison with the geometric value $W \approx 250$ nm. A similar analysis can be carried out for the data reported in Ref. [40] for their vanadium-based device.

Next, we analyze the experimental data reported for the efficiency. In Ref. [40], Moodera and collaborators fabricated thin-film superconductors with one edge purposefully patterned in order to achieve a strong diode effect. For their vanadium device (Fig. 1 in Ref. [40]) they found that $H_{\max} \approx 2.8$ Oe, while from the field dependence of the critical current, we estimate that $H_R^* \approx 2.5$Oe (we identify the weaker edge on the right). Correspondingly, they report that the diode efficiency is maximal for $H \approx H_{\max}$, see their magenta line in Fig. 1(c). This is in agreement with our theoretical results for a diode device where the maximum in η is pinned to the cusp in $I_c(H)$ at $H_{\max}$.

In Ref. [32], the edges of the $NbSe_2$ thin film have not been patterned. They find that $H_{\max} \approx 10$ mT. This is appreciably smaller than the field $H_R^* \approx 25$ mT that we estimate from their Fig. 1(f). In addition, they reported a maximal diode efficiency at a magnetic field $H_\eta \approx 35$ mT, larger than both $H_{\max}$ and H_R^*, in agreement with our theory for devices with $H_{\max} < H_R^* < H_\eta$. Based on this finding, i.e., different peak fields for $I_c(H)$ and $\eta(H)$, the authors concluded that this would rule out a vortex-based mechanism for the superconducting diode effect. Our analysis tells instead that this finding is perfectly consistent with our 2D critical state model that explains the diode behavior in terms of weakly asymmetric surface barriers.

The analysis that led to Eqs. (32), (33), and (34) was carried out under the assumption of symmetric bulk pinning. Dropping this condition and assuming asymmetric bulk pinning with $H_{p,L} \neq H_{p,R}$, a finite diode efficiency can be realized at large fields, see Eq. (30). Furthermore, it turns out that for a sufficiently large bulk asymmetry, the maximum $\eta_{\max}$ can be realized in the tails at large fields rather than at H_η or $H_{\max}$. Moreover, a bulk ratchet effect can give rise to interesting sign reversals of the diode efficiency [38,57,65–67]. Within our 2D critical state model, such a sign change is naturally explained in terms of opposite asymmetries of surface and bulk pinning, i.e., $H_{s,L} > H_{s,R}$ but $H_{p,R} > H_{p,L}$. Indeed, since low and large field behaviors are dominated by surface and bulk, respectively, their change in asymmetry produces a sign change in η as the field H increases.

IV. MAGNETIC PROPERTIES OF THE CRITICAL STATE

We now turn our focus to the magnetic response of 2D thin films with $d \ll \lambda$. We determine the magnetic moment $m(H)$ and study the hysteretic trace for a full sweep $H = 0 \to H_0 \to -H_0 (\to H_0)$ of the magnetic field along the $I = 0$ axis in Fig. 2. The magnetic moment is generated from the currents

flowing inside the superconductor and is thus related to the self-field $\mathbf{B}_{\rm self}$ discussed in Eq. (2). As previously announced in Sec. II, magnetization effects are small but nonetheless measurable with sufficiently sensitive techniques, see the discussion in Sec. V below. Moreover, our study of the magnetic response will reveal interesting vortex configurations, such as coexisting vortex and antivortex domains, that should be accessible to magnetic imaging techniques such as, e.g., the SQUID-on-tip [68].

Standard magnetostatics tells that the magnetic moment $\mathbf{m}$ of a current distribution $\mathbf{j}$ is given by the integral

$$\mathbf{m} = \frac{1}{2c}\int d^3\mathbf{r}\,[\mathbf{r}\times\mathbf{j}(\mathbf{r})], \tag{35}$$

or equivalently, after integration by parts,

$$\mathbf{m} = \frac{1}{4\pi}\int d^3\mathbf{r}\,[\mathbf{B}(\mathbf{r})-\mathbf{H}], \tag{36}$$

where $\mathbf{B}$ is the induction in the film and $\mathbf{H}$ the external field. While our approximation $\mathbf{B}\approx\mathbf{H}$ was appropriate for the calculation of the current density profile $i(x)$, here, we have to consider the small difference between B and H as produced by the current density profile $i(x)$. Although a magnetization experiment is usually carried out with a squarish sample $W\times W$, here, we keep our 1D geometry $W\times L$ with $L\gg W$ of an elongated film in a perpendicular field to avoid going to a 2D description of the sheet current density $\mathbf{i}(\mathbf{R})$. The latter flows along y and we find the magnetic moment m directed along z from (35) to read

$$m = \frac{L}{c}\int_{-W/2}^{W/2} dx\,x\,i(x) = \frac{dL}{4\pi}\int_{-W/2}^{W/2} dx\,[B(x)-H], \tag{37}$$

where we have included a factor 2 in order to account for the contribution from currents parallel to $\pm x$ at the far edges $y=\pm L/2$ of the sample. Indeed, this last contribution is identical to the contribution from currents parallel to $\pm y$ and thus contributes a factor two, in agreement with the result (36) for the total magnetic moment [12].

Accounting for the presence of vortices within the type-II film leads to a hysteretic behavior of the magnetic moment $m(H)$. Below, we will first consider the magnetic moment of a pristine (vortex-free) sample in a magnetic field that is ramped up from zero to $H_0 > H_s$, entering the mixed state at the penetration field H_s. In a second step, we will reverse the field at a value H_0 with vortices trapped within the film and analyze the completion of a full loop in the magnetic moment $m(H)$. We will restrict our analysis to the case of a symmetric thin film with identical surface barriers and symmetric bulk pinning.

A. Magnetic moment: increasing fields

We start with ramping up the external field from zero, as typical in a zero-field cooled (ZFC) experiment. For fields smaller than the surface penetration field H_s, the thin film is in the Meissner state and $i(x)$ is given by Eq. (5). Inserting the result into the expression (37), we obtain the magnetic moment in the absence of vortices,

$$m(|H|<H_s) = -\frac{dWL}{48\pi}\frac{W^2}{\lambda^2}H. \tag{38}$$

The induction B produced by the current density $i(x)$ extends a distance of scale W in both the x and z directions and hence resembles the response of a cylinder of diameter W and length L. Such a cylinder produces the Meissner response $m_{\rm cyl} = -W^2LH/8$ (including a demagnetization factor $n=1/2$ for a cylinder in a perpendicular field H) and expressing the result (38) in terms of the $m_{\rm cyl}$, we find that

$$m(|H|<H_s) = \frac{W}{3\pi\lambda_\perp}m_{\rm cyl}. \tag{39}$$

One should appreciate that the result (39) is quite large, owing to the fact that we deal with a film in a *perpendicular* field. Indeed, the response of the film of dimension $W\times W$ produces a similar moment as that of a cube with dimensions W and there is no geometric reduction. This is different for a film in *parallel* field, where the moment is down by the geometric factor d/W. The only reduction in (39) is by the factor $W/\lambda_\perp \ll 1$ that originates from the reduced screening $\lambda\to\lambda_\perp$ due to the small thickness $d\ll\lambda$ in combination with a restricted film width $W\ll\lambda_\perp$. For the experiments discussed in Sec. III C above, sample sizes are about 20 μm and 10 μm in Refs. [32] and [40], respectively, while $\lambda_\perp\approx 80$ μm and 5 μm, hence the ratio $W/\lambda_\perp$ is of order 0.1–1.

For fields larger than H_s, two symmetric vortex boxes $|x|\in[x_i,x_o]$ as described in Eq. (9) form within the superconductor, see Fig. 6, giving rise to the current density profile shown in Fig. 1(c). Inserting the (antisymmetric) current density profile

$$i(x) = -\frac{cdH}{4\pi\lambda^2}\begin{cases} x, & 0<x\leqslant x_i(H),\\ x_i(H), & x_i(H)\leqslant x\leqslant x_o(H),\\ x_i(H)+[x-x_o(H)], & x_o(H)<x,\end{cases} \tag{40}$$

into the expression Eq. (37) results in

$$\begin{aligned} m(H) = -\frac{dL}{2\pi\lambda^2}H\Bigg[&\int_0^{x_i} dx\,x^2 + x_i(H)\int_{x_i}^{x_o} dx\,x\\ &+[x_i(H)-x_o(H)]\int_{x_o}^{W/2} dx\,x\\ &+\int_{x_o}^{W/2} dx\,x^2\Bigg], \end{aligned} \tag{41}$$

we arrive at the magnetic moment of the mixed state,

$$\begin{aligned} m(H>H_s) &= -\frac{dWL}{48\pi}\frac{W^2}{\lambda^2}\left[-\frac{H}{2}+\frac{H}{2}\left(1-\frac{2H^*}{H}\right)^3\right.\\ &\quad\left.-\frac{H}{2}\left(\frac{H_p}{H}\right)^3+\frac{3}{2}H_s\right]\\ &= -\frac{dWL}{48\pi}\frac{W^2}{\lambda^2}\left[\frac{6(H^*)^2}{H}-\frac{4(H^*)^3+H_p^3/2}{H^2}\right.\\ &\quad\left.+\frac{3}{2}H_p\right], \end{aligned} \tag{42}$$

and antisymmetric in H. The (negative) magnetic moment $m(H)$ as a function of increasing magnetic field H is shown as a solid-black line in Fig. 7 for $H_p = H_s/2$. For moderate bulk pinning strengths $H_p < H_s/\sqrt{3}$, see below, the magnetic

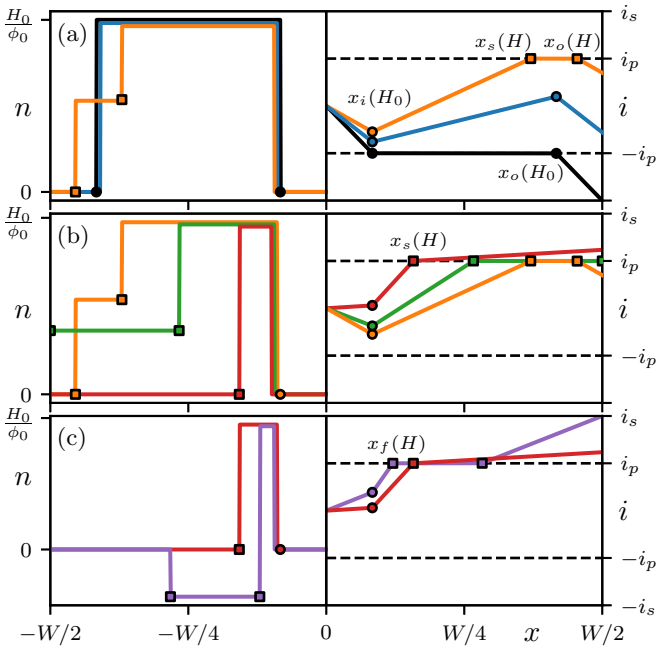

FIG. 6. Vortex and current densities $n(x)$ (left) and $i(x)$ (right) across a symmetric 2D thin film with $H_p = H_s/2$ for a magnetic field decreasing after a field reversal at $H_0 = 2(H_s + H_p)$. The corresponding magnetic moments $m(H)$ are marked in Fig. 7, with the colored dots corresponding to the different fields H in the present figure. The vortex and current density profiles at H_0 are shown in black. Vortices occupy the region $|x| \in [x_i(H_0), x_o(H_0)]$ with edges (circles) given by Eq. (9). (a) As the magnetic field is decreased from H_0 (blue lines), vortices initially cannot move and $n(x)$ is unchanged (overlaping density lines are artificially shifted for clarity); the corresponding current density $i(x)$ assumes a positive slope [$\propto -(H - H_0)$, see Eq. (4)] within the vortex box. (b) As H is decreased below H_1 [Eq. (48), orange lines], the outermost vortices rearrange to form a new region $|x| \in [x_s(H), x_o(H)]$ (squares) with lower density $n(x) = H/\Phi_0$ but overall conserved vortex number; edges (marked by squares) are given by Eqs. (49) and (51) and the current density is constant and equal to i_p. Decreasing H below H_2 [Eq. (52), green lines], the outer boundary of the vortex box touches the sample edges and vortices start leaving the sample. (c) For negative fields $H < 0$ (red lines), vortices stay trapped close to the center of the film for $|x| \in [x_i(H_0), x_s(H)]$. Antivortices [shown with negative density $n(x)$] start entering the sample when $H \leqslant H_3$ [Eq. (53), purple lines] and reside next to the original vortices in the region $|x| \in [x_f(H), x_o(H)]$ (squares). Finally, the original vortex domain is completely annihilated and replaced by a corresponding antivortex box at $H = -H_0$.

moment m depends on H nonmonotonically: At small fields $|H| \leqslant H_s$, $-m(H)$ is dominated by the surface barrier contribution and displays a maximum at the onset H_s of the mixed state with

$$m_s \equiv m(H_s) = -\frac{dWL}{48\pi}\frac{W^2}{\lambda^2}H_s. \tag{43}$$

At large fields $H \gg H_s$, the bulk pinning contribution takes over as $m(H)$ approaches the asymptotic value

$$m(H \to \infty) = -\frac{dWL}{32\pi}\frac{W^2}{\lambda^2}H_p. \tag{44}$$

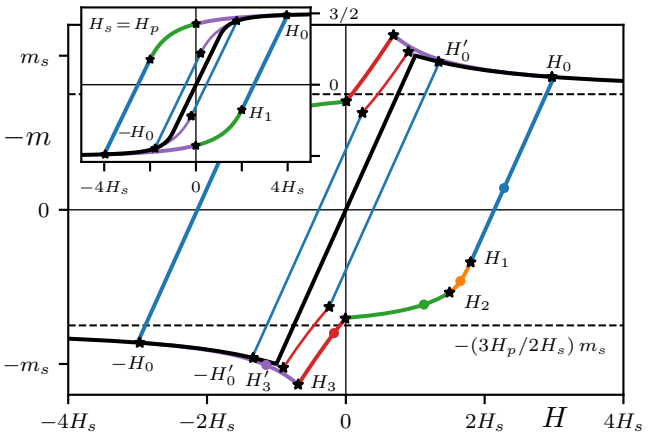

FIG. 7. Negative magnetic moment of a 2D thin-film superconductor with $H_p = H_s/2$ for different reversal fields H_0: thick lines for $H_0 = 2(H_s + H_p)$, thin lines for $H_0' = 0.9(H_s + H_p)$. The colored dots in the large loop identify the fields corresponding to the vortex and current density profiles in Fig. 6; black stars mark the fields $H = 0$ and $H_{0,1,2,3}$ where vortex boxes undergo changes. While ramping up the magnetic field (black line) from the pristine state, the magnetic moment grows linearly with H according to Eq. (38) until vortices first penetrate inside the film at $|H| = H_s$ where $m(H)$ displays a kink, see Eq. (47). The magnetic moment in the mixed state is given by Eq. (42) and saturates to a constant $(3H_p/2H_s)m(H_s)$ given by bulk pinning at large fields H. Decreasing the magnetic field after reversal at H_0, the moment $m(H)$ follows the Meissner slope until H_1 where the vortex density profile starts changing, first keeping the vortex number conserved (orange), then vortices leave the system (below H_2, green) and hold to a thinner box close to the center (below $H = 0$, red). Subsequently, antivortices enter the sample for negative field values $H \leqslant H_3 < 0$ and progressively annihilate trapped vortices (purple) until all vortices have been replaced by antivortices upon reaching $-H_0$. Reversing the field at a smaller value $H_s < H_0' < H_s + H_p$ removes the orange and green intermediate regimes of the loop, with blue and red lines joining at H_1. The top left inset shows the magnetic moment (in units of m_s) at strong bulk pinning $H_p = H_s$.

As shown in Fig. 7, the magnetic moment displays a kink corresponding to a finite jump in the derivative when vortices first penetrate. This jump in $\partial_H m$ can be quantified using Eqs. (38) and (42) by comparing the left and right derivatives of the magnetic moment at H_s,

$$\partial_H m|_{H_s^-} = -\frac{dWL}{48\pi}\frac{W^2}{\lambda^2} \tag{45}$$

and

$$\partial_H m|_{H_s^+} = \frac{dWL}{96\pi}\frac{W^2}{\lambda^2}\left[1 - 3\frac{H_p^2}{H_s^2}\right], \tag{46}$$

yielding the jump

$$\partial_H m|_{H_s^+} - \partial_H m|_{H_s^-} = \frac{dWL}{32\pi}\frac{W^2}{\lambda^2}\left[1 - \frac{H_p^2}{H_s^2}\right]. \tag{47}$$

For negligible bulk pinning $H_p \ll H_s$, we find the universal result that the right derivative (46) is minus half the left value (45). For larger fields H_p, the absolute value of the

right derivative becomes smaller, until it changes sign at $H_p = H_s/\sqrt{3}$. For stronger pinning $H_p > H_s/\sqrt{3}$, the magnetic moment changes monotonically with H, with the kink in $m(H)$ disappearing as $H_p \to H_s$, see the inset of Fig. 7. For larger pinning strengths $H_p > H_s$, the surface barrier does not play any role, as the effective penetration of vortices inside the thin film is determined by the field H_p at which they start moving. This situation can thus be reduced to the case $i_s = i_p$ and is described by Eqs. (38) and (42) by substituting H_s with H_p.

B. Magnetic moment: decreasing fields

After increasing the field in a pristine film, we reverse H at the value H_0. We will mainly focus on the situation where surface pinning is dominant, i.e., $H_s > H_p$. Reversing the field in the Meissner region $H_0 \leqslant H_s$, the film responds reversibly. For a reversal field $H_0 > H_s$, vortices occupy a finite portion of the thin film and do not immediately leave the sample upon decreasing the magnetic field, see Fig. 6 showing the current density $i(x)$ and vortex density $n(x)$ profiles in the right and left halves of the film, respectively. The system shows memory effects with the magnetic moment deviating from Eq. (42), resulting in an hysteretic $m(H)$ loop as shown in Fig. 7.

The current distribution across the thin film along the irreversible part of the magnetic loop can be obtained by integrating the Maxwell-London equation (4) with the appropriate vortex distribution $n(x)$, see Fig. 6. Inserting the resulting current distribution $i(x)$ into the equation (37) for the magnetic moment $m(H)$ then produces the curves shown in Fig. 7. To benefit the reader, we will leave the lengthy but straightforward derivations of the analytical results behind these figures to the Appendix B and focus here on understanding the irreversible behavior of $n(x)$, $i(x)$, and $m(H)$ from the underlying interplay of surface barrier—and bulk pinning effects.

For a magnetic field H just below H_0, the magnitude of the current density in the vortex box drops below i_p. Due to pinning, the vortex density $n(x)$ then remains unchanged from the one at H_0 and assumes the value $n_0 = H_0/\Phi_0$ within the vortex boxes $|x| \in [x_i(H_0), x_o(H_0)]$, see Eq. (9), and zero elsewhere. This is shown on the left part of Fig. 6 with the vortex density $n(x)$ at the reversal field H_0 (black line) overlapping with the one at H (blue line). The Maxwell-London equation (4) then tells that the current $i(x)$ displays a negative slope $\propto -H$ in the vortex-free region and a positive slope $\propto -(H - n\Phi_0) = -(H - H_0)$ in the vortex boxes, see the blue line in the right part of Fig. 6; the corresponding vortex and current density profiles are given by Eqs. (B1) and (B2). Remarkably, and differently from the critical state in the bulk, vortices in this configuration are subject to a finite current density i of magnitude smaller than i_p. In this range of magnetic fields, the magnetic moment is given by Eq. (B3) that depends linearly on H with the Meissner slope (38), see the blue lines in Fig. 7 (with corresponding results at $-H$).

The above state persists as long as vortices do not move away from their original positions, i.e., as long as the current density profile $i(x)$ within the vortex box (that has positive slope) remains in the undercritical domain with $-i_p < i(x) < i_p$. As the magnetic field is lowered from H_0, this condition is first broken when $i(x_o(H_0)) = i_p$, i.e., when H takes the value

$$H_1 = \frac{H_0 - (H_s + H_p)}{H_0 - (H_s - H_p)} H_0 \tag{48}$$

that determines the transition from the blue to the orange curves in Figs. 6 and 7. Below H_1, the vortex density profile $n(x)$ is changed as the vortices at the outer edge of the box move under the critical force $i = i_p$ from their original position $x \leqslant x_o(H_0)$ towards the edge. The vortex box thus divides into high- and low-density parts with densities $n_0 = H_0/\Phi_0$ and $n = H/\Phi_0$, resulting in a two-stage vortex box with a density step at $x_s(H)$ and inner/outer edges at $x_i(H_0)$ and at $x_o(H)$. The position $x_s(H)$ derives from tracing the current profile $i(x)$ from $x = 0$ to $x_i(H_0)$ (with slope $\propto -H$) to the point $x_s(H)$ [with slope $\propto -(H - H_0)$] where it reaches the critical value i_p; the condition $i(x) = i_p$ defines the location

$$x_s(H) = \frac{W}{2} \frac{2H_p}{H_0 - H} \tag{49}$$

of the density step. As long as the resulting two-stage vortex box $[x_i(H_0), x_s(H)]$ with density n_0 and $[x_s(H), x_o(H)]$ with density n does not extend to the film boundary, the total number of vortices remains conserved. To find the box's outer edge $x_o(H)$, we impose the condition for vortex number conservation in the form

$$\frac{H_0}{\Phi_0}(x_o(H_0) - x_i(H_0)) = \frac{H_0}{\Phi_0}(x_s(H) - x_i(H_0)) + \frac{H}{\Phi_0}(x_o(H) - x_s(H)), \tag{50}$$

yielding

$$x_o(H) = \frac{W}{2} \frac{H_0 - (H_s + H_p)}{H}. \tag{51}$$

The current density inside the region $|x| \in [x_s(H), x_o(H)]$ is identical to $\pm i_p$ and assumes a linear slope $\propto -H$ between $\pm x_o(H)$ and the edges $\pm W/2$ of the thin film. The corresponding vortex and current densities are given by Eqs. (B7) and (B8) and are shown in orange in Fig. 6. Due to the conservation of the total vortex number, the areas below the black and orange curves in the $n(x)$ plot are identical. The magnetic moment $m(H)$ turns nonlinear in the interval $H_2 \leqslant H \leqslant H_1$, see Eq. (B9) and the orange segment in Fig. 7. The boundary H_2 of this domain is determined by the condition $x_o(H) = W/2$ where vortices start leaving the film,

$$H_2 = H_0 - H_s - H_p. \tag{52}$$

At H_2, we enter the next regime where vortices are free to exit the sample and their number is no longer conserved. The corresponding current and vortex densities are shown in green in Fig. 6, with the density $n(x)$ in the inner [outer] vortex box given by $n_0(x) = H_0/\Phi_0$ [$n(x) = H/\Phi_0$]. The inner boundary and the location of the density step in the two-stage box are still given by $x_i(H_0)$ and $x_s(H)$, while the outer boundary is pinned to the edge, $x_o(H) = W/2$; the vortex and current density profiles are given in Eqs. (B10) and (B11). The constant currents $\pm i_p$ flowing in a large part of the sample produce a reduction in the field dependence of the magnetic moment $m(H)$, see Eq. (B12), and the corresponding (green) portion

of the magnetic moment $m(H)$ in Fig. 7 turns more flat. The orange segment between H_1 and H_2 connects smoothly the blue and green segments at larger and smaller fields, with no change in the derivative of $m(H)$ at H_1 and H_2 (but a change in curvature).

Vortices continue leaving the film until $H = 0$; at vanishing field, the density $n = H/\Phi_0$ in the outer vortex box has dropped to zero and all vortices at criticality (i.e., where $i = i_p$) have left the film. For negative fields $H < 0$, a thin vortex box with original density $n_0 = H_0/\Phi_0$ survives in the intervals $|x| \in [x_i(H_0), x_s(H)]$, with $x_s(H)$ still determined by tracing the current profile starting at $x = 0$ and using the condition $i(x) = i_p$, what results in the expression (49) for x_s. In the remaining part $|x| \geqslant x_s(H)$, $i(x)$ changes linearly with positive slope $\propto -H$, see the red lines in Fig. 6 and Eqs. (B13) and (B14) for the vortex and current density profiles. Within the interval $H_3 \leqslant H \leqslant 0$, the magnetic moment $m(H)$ changes close to linearly with field H and is given by Eq. (B15); furthermore, $m(H)$ displays a kink at $H = 0$ and overshoots the maximal Meissner value $m(H_s)$ given in Eq. (43) close to H_3.

The last hysteretic regime along the magnetic loop is encountered when antivortices start penetrating from the film edges. This happens when the above current profile $i(x)$ (traced from $x = 0$, see red line in Fig. 6) touches $\pm i_s$ at $\pm W/2$, resulting in the field

$$H_3 = \frac{H_0 - H_s - H_p}{2}\left[1 - \sqrt{1 + \frac{8H_0H^*}{(H_0 - H_s - H_p)^2}}\right]. \quad (53)$$

The vortex density profile $n(x)$ again splits into two parts, the leftover vortices with density $n_0 = H_0/\Phi_0$ in the region $x_i(H_0) \leqslant |x| \leqslant x_f(H)$ and the incoming antivortices in the region $|x| \in [x_f(H), x_o(H)]$. The vortex–antivortex front $x_f(H)$ and the boundary $x_o(H)$ again derive from tracing the current profile with the appropriate slopes, once from $x = 0$ till cutting $\pm i_p$ and the other time from $W/2$ where $i(\pm W/2) = \pm i_s$ and $i(\pm x_o(H)) = \pm i_p$; the front $x_f(H)$ assumes the role of the step $x_s(H)$ (49) and the boundary $x_o(H)$ is given by (9) with the replacement $H \to -H$.The resulting vortex and current densities are given by Eqs. (B16) and (B17) and are shown in purple in Fig. 6. At $H_3 < 0$, the magnetic moment curve $m(H)$ in Fig. 7 displays another kink and, for sufficiently weak pinning, the slope of $m(H)$ changes sign at H_3 [see Eqs. (45) and (46) for a quantitative analysis of the kink at $H_s > 0$]. Correspondingly, the absolute value of $m(H)$ starts decreasing again, see Eq. (B18) and the purple curves in Fig. 7. Note that the magnitude $|H_3| < H_s$, i.e., antivortices enter the film at a lower field amplitude H_3 as compared with the field H_s for vortex entry. Hence, the presence of vortices inside the film lowers the critical entry field for antivortices.

As shown with the purple line in the left panel of Fig. 6, in this field regime the vortex and antivortex domains are adjacent to one another at $\pm x_f(H)$. With further decreasing field $H < H_3$, the vortex box is gradually shrinking through incoming antivortices—vortex–antivortex annihilation then moves the boundary $x_f(H)$ towards the film center until all vortices have disappeared when reaching $x_i(H_0)$. This happens at $H = -H_0$ where the entire original vortex box produced at H_0 has been replaced by the congruent antivortex box and all memory of the field reversal at H_0 is erased.

Above, we have implicitly assumed that vortex–antivortex annihilation is stabilized at $\pm i_p$, i.e., by bulk pinning. Indeed, the vortex–antivortex attraction quantified by the current density $\sim i_0\xi/s$ at separation s should be (over)compensated by the bulk pinning current i_p at a scale $s \sim a_0$; at very weak bulk pinning, $s \sim i_0\xi/i_p$ grows beyond a_0 and an additional vortex-free region separates the vortex box from the antivortex box.

So far, we have assumed a reversal field H_0 larger than $H_s + H_p$, that implies positive values for the fields H_1 and H_2 given by Eqs. (48) and (52). Reversing the field at smaller fields $H_s < H_0 < H_s + H_p$, we find that $H_1 < 0$ and vortices at $x_s(H)$ immediately leave the film for fields $H \leqslant H_1$. Correspondingly, the intermediate regimes $H_2 \leqslant H \leqslant H_1$ and $0 \leqslant H \leqslant H_2$ are not realized any longer; referring to Figs. 6 and 7 the behavior of $n(x)$, $i(x)$, and $m(H)$ jumps directly from "blue" to "red" at $H = H_1 < 0$. Note that the current distribution $i(x)$ at $H < H_1$ differs from the one at fields larger than H_1 only by the substitution $x_o(H_0) \to x_s(H)$ for the outer boundary of the vortex box.

To conclude this section, let us relax the condition of a strong surface barrier and consider the possibility that bulk pinning prevails with $H_p > H_s$. This corresponds to the scenario where the vortex entry to the film is hampered by bulk pinning and the critical current density i_s does not play any role. As discussed at the end of Sec. III B, this regime is successfully described with the help of the results from this section upon substitution of H_s with H_p. In this limit, the field H_2 reduces to H_1 for any value of H_0, as the original vortex box extends to the sample edges and vortices start leaving the sample as soon as they can move from their original positions when the current density reaches the bulk critical value $\pm i_p$. In addition, $H_3 = 0$ when $H_0 > 2H_p$, while $H_3 = H_1$ when $H_1 < 0$, i.e., for $H_0 < 2H_p$, see the inset of Fig. 7 where $H_p = H_s$. In the first case, the outermost vortices reduce their density as the field is decreased below H_1 (the magnetic moment changes from "blue" to "green" type behavior in Fig. 7, see also Fig. 6), and are gradually replaced by antivortices as H turns negative ("green" to "purple" type behavior). In the second, antivortices start penetrating into the sample as soon as vortices can escape their pinning centers (direct "blue" to "purple" type behavior). As for the previously considered scenario with $H_p < H_s$, vortex and antivortex domains coexist for $-H_0 \leqslant H \leqslant \min(0, H_1)$. Finally, because antivortices replace vortices immediately as these exit the sample at $H = 0$ or $H = H_1$, the magnetic trace $m(H)$ displays no kink upon sweeping the external magnetic field when the surface barrier is weaker than bulk pinning.

V. CONCLUSIONS

We have presented a 2D critical state model that describes the macro-phenomenological properties of 2D thin films with thickness $d \ll \lambda$. The geometrically suppressed screening introduces the characteristic length $\lambda_\perp = 2\lambda^2/d \gg \lambda$ that easily exceeds the film's width W. In such films with $d \ll \lambda$ and $W \ll \lambda_\perp$, the current profile $i(x)$ can be found from a straightforward integration of the Maxwell-London

equation (4) in the absence of self-field effects (3). The driving term in the Maxwell-London equation (4) depends on the vortex density profile $n(x)$ that we find by including both surface barriers governing vortex entry as well as bulk pinning trapping vortices within the film. The solution of the Maxwell-London equation then involves only linear (Meissner state) and constant (mixed state) segments of current density; together with the vortex profile $n(x)$ (made from vortex boxes), these segments are self-consistently combined into the current profile $i(x)$. The results of this 2D critical state model differ pronouncedly from the results of the Bean model describing bulk samples and are quantitatively different from the usual ($d > \lambda$) flat sample macrophenomenology that is dominated by demagnetization- and geometric edge effects.

We have made use of our 2D critical state model to analyze and solve various tasks, the critical current $I_c(H)$ in both symmetric and asymmetric 2D thin films, the determination of the (hysteretic in I) state at arbitrary currents $-I_c < I < I_c$ and (fixed) fields H, and the hysteretic (in H) magnetic moment $m(H)$. In the resulting phenomenology, effects of surface pinning manifest at small fields, specifically a linear cusp in $I_c(H)$, Eq. (16), while bulk pinning manifests in the tails of $I_c(H)$ at large fields, Eq. (17). In asymmetric thin films with edges of different surface pinning strength and/or ratchet type bulk pinning, the current transport is nonreciprocal, with the peak maximum in $I_c(H)$ shifted away from zero to $H_{\max}$, see (25). This nonreciprocity lends itself to the fabrication of superconducting diodes; here, we have extended previous analysis [27,49,50] to include the effect of bulk pinning and have determined the diode's efficiency. The comparison with recent experiments shows good agreement between data and theory.

Alternative mechanisms have been proposed that produce a superconducting diode effect [59–63]. However, the very nature of the effect involves the appearance of a finite voltage, and the question about the origin of this voltage has to be asked first. In a type II superconductor, a finite voltage is predominantly due to vortex motion—depairing physics only appears at higher current drives where vortices have already depinned. It is thus important to understand why vortex physics can be ignored when attributing the SDE to more exotic superconducting states.

The magnetic moment $m(H)$ of 2D thin films has remained uncharted territory so far, both with respect to experiment and theory. While the induced current $i(x)$ in the film is small (and can be neglected in the self-field contribution (3) to the Maxwell-London equation), it is this small current that determines the magnetic moment $m(H)$ in (37). When surface pinning dominates over bulk pinning, vortex entry into the film manifests as a cusp in the magnetic moment curve $m(H)$, see Eq. (47). Upon reversing the field in the mixed state at H_0, the trapped vortex box evolves in several steps, with field regimes where the box remains invariant, where it splits into two adjacent boxes, where vortices leave as the box reaches the film's edge and the box shrinks, where antivortices annihilate the remaining shrunk box, until all the original vortex box at the field reversal H_0 has transformed to a corresponding antivortex box at $-H_0$ and all memory of the initial state has been lost.

In our study, we have made several assumptions that may be overcome in future work. For example, we have assumed that the external current I is fed homogeneously to the film. In a real sample, although, the contact may feed the current to the film in a nonuniform way, particularly when the contact is small compared to the film width. Second, we remind that our calculation for the magnetic loop has focused on symmetric films, that is the exception rather than the rule as asymmetry in surface pinning occurs quite naturally. Such asymmetry, although, introduces further complexity into the vortex and current density profiles, that may be worth analyzing once experiments are being carried out. Furthermore, we have kept the stripe geometry in the calculation of the magnetic moment for simplicity, although typical samples in this type of experiments are rather of squarish shape. While we expect the main features (various vortex regimes with cusps, kinks, and smooth crossovers separating them) in the hysteretic loop $m(H)$ to be preserved, the detailed trace may be modified depending on the exact shape of the sample, square, rectangular, or more irregular; numerical techniques appropriate to tackle this type of problem can be found in Refs. [69,70].

An interesting question is whether and how the current profile $i(x)$ and the magnetic moment m could be measured in an experiment, as these quantities are small due to the film's small thickness d; furthermore, the film dimensions (in the μm) range are usually quite small. Assuming typical current densities $j \sim 10^6$ Acm^{-2} and thicknesses d in the few nanometer range, we expect local (parallel) fields $B_x \sim (2\pi/c) i_y$ of order a fraction of a Gauss (e.g., 0.3 G for $d = 5$ nm). A correspondingly high sensitivity is provided by the three-junction SQUID on tip (3JSOT) device introduced in Ref. [71] that has been developed for simultaneous measurement of parallel and perpendicular (to the film) field components. Using the 3JSOT as a scanning probe at a distance of order 10 nm above the film, one should be able to image the current density profile $i_y(x) = i(x)$ in typical samples with widths from 100 nm to 10 μm, given the reported ac resolution of the device on the order of 0.1 G. Using similar sensitive devices allows to measure the magnetic moment m of the film, e.g., via integration of the magnetization $M_z(\mathbf{R})$ map [72].

Another concern is the application of the macrophenomenological theory to mesoscopic sized samples that appear quite numerously in recent experimental setups. Considering the relevant field scale H_s, see Eq. (7), we can extract a relevant vortex distance $a_0 \sim \sqrt{\xi W}$, that produces a small number $W/a_0 \sim \sqrt{W/\xi}$ of vortex rows. With typical values $\xi \sim 10$ nm and $W \sim$ μm, we arrive at order 10 vortex rows and our simple averaging in a vortex profile $n(x)$ may have to be reconsidered. Nevertheless, our results provide a simple and effective first description of the phenomenology of 2D thin films, and improving upon our macro-modelling may require numerical tools.

An interesting observation concerns the nonuniform (linear) current profile $i(x)$ that we found in the 2D thin film, a result deriving from the reduced screening. This linear profile contrasts to the usual constant current density profile in the bulk Bean model and may bear interesting consequences when driving the film beyond critical. Indeed, in the

dissipative state, flux-flow or normal, we expect a uniform current that is driven by a (uniform) electric field. The transition from the superconducting to the dissipative state in the film then is associated with a sudden rearrangement of the current profile that is expected to give rise to voltage jumps and hysteretic effects.

ACKNOWLEDGMENTS

We thank Mikhail Feigelman, Alex Gurevich, and Jagadeesh Moodera for inspiring discussions. We acknowledge financial support of the Swiss National Science Foundation, Division II and the support of the EU Cost Action CA16218 (NANOCOHYBRI).

APPENDIX A: CURRENT DENSITY PROFILE IN THE MIXED STATE

We derive the current density profile in the mixed state and obtain the relevant expressions for the vortex box geometries that are relevant to Sec. II C. We consider positive magnetic fields H, such that vortices accumulate towards the right of the superconductor when $I > 0$. We first consider the situation where the superconductor is prepared at vanishing bias current $I = 0$, as discussed in Sec. II C 1 and subsequently analyze the scenario where the bias current I is decreased from an $I_c(H)$, see Sec. II C 2.

1. Increasing current from $I = 0$

a. Fields $H \leqslant H_s$

The current density profiles for states prepared from an initial configuration with $I = 0$ are shown in Fig. 3. For small fields $H \leqslant H^*$, the superconductor remains in the Meissner state for all values of the current I and no hysteretic effect is present. For larger fields $H^* \leqslant H \leqslant H_s$, the superconductor is in the Meissner state when $I \leqslant I_s(H)$, see Eq. (19), and enters the mixed state at larger currents when $i(-W/2) = i_s$ and vortices penetrate from the left edge of the film. For $I > I_s(H)$, the current density profile at the left of the film drops linearly from i_s,

$$i(x) = i_s - \frac{cd\,H}{4\pi\lambda^2}\left(x + \frac{W}{2}\right), \quad -W/2 \leqslant x \leqslant x_0, \tag{A1}$$

and pushes the vortices to the right; these accumulate in a box $x \in [x_0, x_1]$ with constant current and vortex densities $i(x) = i_p$ and $n(x) = H/\Phi_0$. The expression for the left boundary x_0 of the vortex box is found by equating $i(x)$ in (A1) to i_p and we find

$$x_0(H) = -\frac{W}{2}\left(1 - \frac{2H^*}{H}\right), \tag{A2}$$

independent of I and identical to $-x_o(H)$ in Eq. (9) with $H_s - H_p$ rewritten as $2H^*$, see Eq. (14); the result is applicable in the wide field interval $|H| \in [H^*, H_{c2}]$ where it takes values between $W/2$ and $-W/2 + \xi$.

The vortex box extends between x_0 and x_1; to the right of the box, $x > x_1$, the current density profile again drops linearly from i_p,

$$i(x) = i_p - \frac{cd\,H}{4\pi\lambda^2}(x - x_1), \quad x_1 \leqslant x \leqslant W/2, \tag{A3}$$

and the constraint of fixed bias current $I = \int i(x)dx$ fixes x_1, that reads

$$x_1(H, I > I_s) = W\left[\frac{1}{2} - \sqrt{\frac{H_p}{H}\left(1 + \frac{(H^*)^2}{HH_p}\right) - \frac{I}{I_p}}\right], \tag{A4}$$

or, after using equation (17) for $I_c(H)$,

$$x_1(H, I > I_s) = W\left[\frac{1}{2} - \sqrt{\frac{H_p}{H}\frac{I_c(H) - I}{I_p}}\right], \tag{A5}$$

which touches $W/2$ when $I = I_c(H)$. The left and right boundaries (A2) and (A4) are shown as black dots in Fig. 3(d).

b. Fields $H > H_s$

For larger fields $|H| > H_s$ and vanishing bias current $I = 0$, two symmetric vortex boxes (where $i = \pm i_p$) are present inside the superconductor, see Fig. 1(c), the left (right) one extending from $x_0 = -x_o$ to $x_1 = -x_i$ ($x_2 = x_i$ to $x_3 = x_o$), see Eq. (9). Upon increasing the bias current I, the left box expands to the right as new vortices enter from $-W/2$, while the right one shifts towards $W/2$ with conserved vortex number as the vortices therein are trapped.

To find the positions of the four edges of the vortex boxes, we impose that the current density profile $i(x)$ [involving linear and constant portions as follows from Eq. (4)] is continuous and the total transport current is fixed to $I = \int dx\, i(x)$. The condition $i(-W/2) = i_s$ fixes

$$x_0(H) = -\frac{W}{2}\left(1 - \frac{2H^*}{H}\right) \tag{A6}$$

and the conserved vortex number in the right box, $x_3(I, H) - x_2(I, H) = x_o(H) - x_i(H)$ together with Eq. (9) requires that

$$x_3(I, H) = x_2(I, H) + \frac{W}{2}\left(1 - \frac{H_s}{H}\right). \tag{A7}$$

Finally, the linear portion of $i(x)$ between x_1 and x_2 connects the critical current densities i_p and $-i_p$, hence

$$x_2(I, H) = x_1(I, H) + \frac{W}{2}\frac{2H_p}{H}, \tag{A8}$$

which, when replaced to Eq. (A7), yields

$$x_3(I, H) = x_1(I, H) + \frac{W}{2}\left(1 - \frac{2H^*}{H} + \frac{H_p}{H}\right). \tag{A9}$$

Integrating the profile $i(x)$, we find the total current

$$I = i_p(x_1 + x_2) + \frac{1}{2}\frac{cdH}{4\pi\lambda^2}\left(x_0 + \frac{W}{2}\right)^2 - \frac{1}{2}\frac{cdH}{4\pi\lambda^2}\left(\frac{W}{2} - x_3\right)^2. \tag{A10}$$

The above equations (A6)–(A10) determine the four box boundaries x_0, x_1, x_2, x_3 as functions of given field H and

current I; they apply to the regime $I < I_t(H)$, see Eq. (21), where the right box is separated from the right boundary, $x_3 < W/2$. Inserting x_0 from (A6) and $x_3 = W/2$ into (A10), we find the current $I_t(H)$ as given in (21). This result for $I_t(H)$ then allows us to write the results for the box boundaries in a compact form,

$$x_3 = \frac{W}{2}\left(1 + \frac{2H_p}{H}[1 - S(H,I)]\right), \tag{A11}$$

$$x_2 = \frac{W}{2}\left(\frac{H_s}{H} + \frac{2H_p}{H}[1 - S(H,I)]\right), \tag{A12}$$

and

$$x_1 = \frac{W}{2}\left(\frac{H_s}{H} - \frac{2H_p}{H}S(H,I)\right), \tag{A13}$$

with

$$S(H,I) = \sqrt{1 + \frac{H}{H_p}\frac{[I_t(H) - I]}{I_p}}. \tag{A14}$$

The corresponding current density profile is shown in blue in Fig. 3(e) with the edges of the left and right vortex boxes marked by black dots. For $I = I_t(H)$, we have $S = 1$ and $x_3 = W/2$.

For larger currents, vortices start exiting the right box, which gradually shrinks. In this situation, the expression for the total current I simplifies to

$$I = i_p(x_1 + x_2) + \frac{1}{2}\frac{cdH}{4\pi\lambda^2}\left(x_0 + \frac{W}{2}\right)^2 \tag{A15}$$

and using the relations (A6) and (A8), the new edges of the vortex boxes are found to be

$$x_2 = \frac{W}{2}\left(1 - \frac{I_d(H) - I}{I_p}\right) \tag{A16}$$

and

$$x_1 = \frac{W}{2}\left(1 - \frac{2H_p}{H} - \frac{I_d(H) - I}{I_p}\right), \tag{A17}$$

Similar as above, we have made use of the expression (22) for $I_d(H)$, which is to be obtained by the condition $x_2 = W/2$ for the complete disappearance of the right vortex box and inserting the expressions for x_0 and x_1 into (A15). The current density profile for $I_t(H) < I \leqslant I_d(H)$ is shown in magenta in Fig. 3(e). Finally, when $I = I_d(H)$, the right vortex box disappears as $x_2 = W/2$, and the mixed state displays a single vortex box described by Eqs. (A2) and (A5) above.

2. Decreasing current from $I_c(H)$

The presence of vortices leads to hysteretic effects, changing the film's behavior upon decreasing the bias current I from $I_c(H)$ as compared to increasing I from zero.

After the state preparation at I slightly below $I_c(H)$ for fields $H > H^*$, vortices remain trapped in their position as long as the absolute value of the local current density does not exceed i_p. Upon decreasing the bias current I, the current distribution is therefore shifted rigidly towards smaller values, see the upper black and red curves in Fig. 4(b), until the current density in the vortex box reaches $-i_p$—this happens when $I = I_c(H) - 2I_p \equiv I_r(H)$, see the black-dashed line in (a). Beyond this point, vortices start rearranging and the vortex box shifts to the left, while maintaining its width and total vortex number. Correspondingly, a new vortex-free region with linear current density profile is formed close to the right edge [lower red curve in (b)]. In this regime, the edges of the vortex box are found by imposing that the current density profile is continuous and carries the total current

$$I = -i_pW + \frac{1}{2}\frac{c\,dH}{4\pi\lambda^2}\left(x_0 + \frac{W}{2}\right)^2 - \frac{1}{2}\frac{c\,dH}{4\pi\lambda^2}\left(\frac{W}{2} - x_1\right)^2. \tag{A18}$$

The distance $x_1 - x_0$ does not depend on I and its evaluation at $I_c(H)$ [where x_0 is given by (A6) and $x_1 = W/2$] produces the condition $x_1 - x_0 = W(1 - H^*/H)$. Combining this result with Eq. (A18), we find that

$$x_0 = -\frac{W}{2}\left(1 - \frac{2H^*}{H} + \frac{H_p}{H^*}\frac{[I_r - I]}{I_p}\right) \tag{A19}$$

and

$$x_1 = \frac{W}{2}\left(1 - \frac{H_p}{H^*}\frac{[I_r - I]}{I_p}\right). \tag{A20}$$

The edges of the vortex box in the regime $I < I_c(H) - 2I_p = I_r$ are marked with black dots in Fig. 4(b). Finally, when $I = -I_c(H)$, the vortex box touches the left edge of the sample, while $i(W/2)$ reaches $-i_s$, and the system has lost any memory of the preparation at $I_c(H)$.

APPENDIX B: MAGNETIC MOMENT FOR A 2D THIN-FILM SUPERCONDUCTOR

Sweeping the magnetic field down from a reversal value $H_0 > H_s$, the current distribution across the thin film depends on the vortex density via the Maxwell-London equation (4), with the latter to be determined by the interplay of surface and bulk pinning. Along the magnetic loop, both the current and vortex profiles change shape as shown in Fig. 6 with separate colors. Inserting the current density profiles $i(x)$ into the definition (37) for the magnetic moment, we obtain $m(H)$ for the various regimes, as plotted in Fig. 7 using the same color coding. In this Appendix, we present the analytical expressions for the current- and vortex densities and for the magnetic moments as a function of the magnetic field, thus complementing the discussion in Sec. IV B with quantitative results.

a. Fields $H_1 \leqslant H \leqslant H_0$

As the magnetic field is reversed at H_0, vortices stay trapped in their original positions $|x| \in [x_i(H_0), x_o(H_0)]$, see Eq. (9), and the vortex distribution is given by

$$n(x > 0) = \begin{cases} 0, & x \leqslant x_i(H_0), \\ H_0/\Phi_0, & x \in [x_i(H_0), x_o(H_0)], \\ 0, & x > x_o(H_0). \end{cases} \tag{B1}$$

and symmetrically for $x < 0$. This produces the (antisymmetric in x) current distribution

$$i(x>0) = -\frac{cd}{4\pi\lambda^2}\begin{cases} Hx, & x \leqslant x_i(H_0), \\ Hx - H_0\,[x - x_i(H_0)], & x_i(H_0) \leqslant x \leqslant x_o(H_0), \\ Hx - H_0\,[x_o(H_0) - x_i(H_0)], & x > x_o(H_0), \end{cases} \tag{B2}$$

that involves three linear in x segments as shown with the blue line in Fig. 6. Integrating the current density profile as prescribed in Eq. (37) [see also Eq. (41)], we obtain the magnetic moment (shown in blue in the magnetic loop in Fig. 7)

$$m(H) = -\frac{dWL}{48\pi}\frac{W^2}{\lambda^2}\left[H + \frac{H_0}{2}\left(1 - \frac{2H^*}{H_0}\right)^3 - \frac{H_0}{2}\left(\frac{H_p}{H_0}\right)^3 - \frac{3}{2}(H_0 - H_s)\right]. \tag{B3}$$

With reference to the piecewise current density integral, cf. (41), the first and last terms in (B3) originate from the film edge at $W/2$, while the second and third term derive from the vortex box boundaries at $x_o(H_0)$ and $x_i(H_0)$, respectively, see Eq. (9) and use $H_s - H_p = 2H^*$. Making use of the result (42) for the mixed-phase moment $m(H > H_s)$ in the main text, we can reexpress the above result in the form

$$m(H) = m(H_0) - \frac{dWL}{48\pi}\frac{W^2}{\lambda^2}(H - H_0) \tag{B4}$$

to find that the Meissner slope is retraced downwards from the point $(H_0,\ m(H_0))$ in the m–H diagram. This result can be easily understood by inspection of the current density profile (B2) [see also Fig. 6(a)]: Although vortices are present, they are pinned with a fixed density $n_0 = H_0/\Phi_0$ and box boundaries $x_i(H_0)$ and $x_o(H_0)$ that do not depend on H. As a consequence, the derivative $\partial_H i = -(cd/4\pi\lambda^2)\,x$ extends uniformly over the entire width of the film, see Eqs. (4) and (5), that result in a Meissner response.

The vortex distribution changes when the outermost vortex can move again, i.e., for

$$i(\pm x_o(H_0), H_1) = \pm i_p \tag{B5}$$

from which we find the field boundary H_1,

$$H_1 = H_0\frac{H_0 - H_s - H_p}{H_0 - H_s + H_p}. \tag{B6}$$

b. Fields $H_2 \leqslant H \leqslant H_1$

Lowering the field below H_1, the outermost vortices rearrange themselves to define a new density profile

$$n(x>0) = \begin{cases} 0, & x \leqslant x_i(H_0), \\ H_0/\Phi_0, & x \in [x_i(H_0), x_s(H)], \\ H/\Phi_0, & x \in [x_s(H), x_o(H)], \\ 0, & x > x_o(H), \end{cases} \tag{B7}$$

and the current distribution reads [we express the bulk critical current i_p by H_p, $i_p = (cd/4\pi\lambda^2)\,H_p\,W/2$]

$$i(x>0) = -\frac{cd}{4\pi\lambda^2}\begin{cases} Hx, & x \leqslant x_i(H_0), \\ Hx - H_0\,[x - x_i(H_0)], & x_i(H_0) \leqslant x \leqslant x_s(H), \\ -H_p\,W/2, & x_s(H) \leqslant x \leqslant x_o(H), \\ -H_p\,W/2 + H\,[x - x_o(H)], & x > x_o(H). \end{cases} \tag{B8}$$

The edges $x_s(H)$ and $x_o(H)$ of the region where vortices redistribute are found by imposing the condition $i(x_s(H)) = i_p$ together with the conservation of vortex number (50), see Eqs. (49) and (51). Together, these conditions provide the results (49) and (51) in the main text. At the field $H_2 = H_0 - H_s - H_p$, cf. Eq. (52), the outer edge reaches the film surface, $x_o(H_2) = W/2$, and vortices start exiting the sample. The current and vortex distributions for fields $H_2 \leqslant H \leqslant H_1$ are shown in orange in Fig. 6 and give rise a nonlinear dependence of the magnetic moment on H (shown in orange in Fig. 7),

$$m(H) = -\frac{dWL}{48\pi}\frac{W^2}{\lambda^2}\left[H + \frac{H}{2}\left(\frac{H_0 - H_s - H_p}{H}\right)^3 + H_p\left(\frac{2H_p}{H_0 - H}\right)^2 - \frac{H_0}{2}\left(\frac{H_p}{H_0}\right)^3 - \frac{3}{2}(H_0 - H_s)\right]. \tag{B9}$$

Again, the first and last terms originate from the film edge $W/2$, the second and third terms derive from $x_o(H)$ and $x_s(H)$ [note that $x_o(H_0)$ as given by Eq. (9) changes to $x_o(H)$ given by Eq. (51) when the box splits], respectively, and the fourth term comes from the inner boundary $x_i(H_0)$. This association of terms with boundaries will repeat itself also in the expressions below. Furthermore, we note that $\partial_H m$ is continuous at H_1: indeed, the derivatives $\partial_H i$ of Eqs. (B2) and (B8) match up, as the interval $[x_s(H), x_o(H)]$ starts appearing only when H drops below H_1 and $Hx_o(H) = (H_0 - H_s - H_p)\,W/2$ is independent of H according to Eq. (51).

c. Fields $0 \leqslant H \leqslant H_2$

Decreasing the magnetic field below H_2, the total vortex number is not conserved as the outermost vortices gradually leave the sample,

$$n(x>0) = \begin{cases} 0, & x \leqslant x_i(H_0), \\ H_0/\Phi_0, & x \in [x_i(H_0), x_s(H)], \\ H/\Phi_0, & x \in [x_s(H), W/2], \end{cases} \tag{B10}$$

with the corresponding critical current densities $i(x) = \pm i_p$ extending to the sample edges. The full $i(x)$ profile reads

$$i(x>0) = -\frac{cd}{4\pi\lambda^2} \begin{cases} Hx, & x \leqslant x_i(H_0), \\ Hx - H_0\,[x - x_o(H_0)], & x_i(H_0) \leqslant x \leqslant x_s(H), \\ -H_p\,W/2, & x > x_s(H), \end{cases} \tag{B11}$$

with $x_s(H)$ still given by Eq. (49). Again, the derivatives $\partial_H i$ of Eqs. (B8) and (B11) match up at H_2: Since $x_o(H) = W/2$ at H_2, the vortex-free region between x_o and $W/2$ disappears and the last region $x > x_o(H)$ of Eq. (B8) is absent. As a result, the derivative $\partial_H m$ is continuous at H_2. This profile remains valid until all vortices in the outermost region $|x| \geqslant x_s(H)$ have left the film, i.e., until $H = 0$. The vortex and current density profiles in the field interval $0 \leqslant H \leqslant H_2$ are shown in green in Fig. 6. As the current density is constant and equal to $\pm i_p$ in a large part of the sample, the magnetic moment depends only weakly on the field in this regime,

$$m(H) = -\frac{dWL}{48\pi}\frac{W^2}{\lambda^2}\left[H_p\left(\frac{2H_p}{H_0 - H}\right)^2 - \frac{H_0}{2}\left(\frac{H_p}{H_0}\right)^3 - \frac{3}{2}H_p\right], \tag{B12}$$

as can be seen by the green curve in Fig. 7. Since the slope in $i(x)$ at $W/2$ is absent, see the green line in Fig. 6 left, there is no linear in H term in Eq. (B12); furthermore, the boundary $x_o(H)$ is absent in this field interval. As discussed in the main text, the above discussion for fields in the interval $0 \leqslant H \leqslant H_1$ is valid as long as $H_1 \geqslant 0$, i.e., when $H_0 \geqslant H_s + H_p$. Else, the field $H_1 < 0$ turns negative and the outermost vortices are expelled from the film as soon as they can move away from their pins.

d. Fields $H_3 \leqslant H \leqslant 0$

Decreasing the field further below $\min(0, H_1)$, the vortex region shrinks together with $x_s(H)$ and the outermost region turns vortex-free,

$$n(x>0) = \begin{cases} 0, & x \leqslant x_i(H_0), \\ H_0/\Phi_0, & x \in [x_i(H_0), x_s(H)], \\ 0, & x > x_s(H). \end{cases} \tag{B13}$$

Correspondingly, the current density is once again linear close to the edges of the sample, with the overall profile taking the form

$$i(x>0) = -\frac{cd}{4\pi\lambda^2} \begin{cases} Hx, & x \leqslant x_i(H_0), \\ Hx - H_0\,[x - x_i(H_0)], & x_i(H_0) \leqslant x \leqslant x_s(H), \\ -H_p\,W/2 + H\,[x - x_s(H)], & x > x_s(H). \end{cases} \tag{B14}$$

These results are valid as long as $i(W/2) \leqslant i_s$, prohibiting antivortices to enter the film, that defines the field H_3 as given by Eq. (53). The corresponding vortex and current densities are shown in red in Fig. 6 and give rise to an approximately linear dependence of the magnetic moment on the field H (see the red segments in Fig. 7),

$$m(H) = -\frac{dWL}{48\pi}\frac{W^2}{\lambda^2}\left[H + \frac{H_0}{2}\left(\frac{2H_p}{H_0 - H}\right)^3 - \frac{3H_0}{2}\frac{2H_p}{H_0 - H} - \frac{H_0}{2}\left(\frac{H_p}{H_0}\right)^3 + \frac{3H_p}{2}\right]. \tag{B15}$$

Note, however, that the Meissner slope is spoiled by the field dependence of $x_s(H)$ in (B14), cf. Eq. (B2) where no such dependence of the vortex density $n(x)$ on H shows up; furthermore, the term $Hx_s(H)$ is responsible for the deviation from the linear dependence of $m(H)$. The association of terms and boundaries in (B15) now involves three terms from $x_s(H)$ and the $x_o(H)$ term is absent.

e. Fields $-H_0 \leqslant H \leqslant H_3$

When antivortices start penetrating into the thin film for $H \leqslant H_3$, neighboring vortex and antivortex domains form (if pinning is sufficiently strong), and the vortex distribution reads

$$n(x>0) = \begin{cases} 0, & x \leqslant x_i(H_0), \\ H_0/\Phi_0, & x \in [x_i(H_0), x_f(H)], \\ H/\Phi_0, & x \in [x_f(H), x_o(H)], \\ 0, & x > x_o(H), \end{cases} \tag{B16}$$

where the density $n(x) = H/\Phi_0$ is negative in the region $x_f(H) \leqslant |x| \leqslant x_o(H)$, $x_o(H) = (W/2)[1 + 2H^*/H)$ follows from (9) with $H < 0$, and the position of the vortex–antivortex front $x_f(H)$ is found the same way as the step position $x_s(H)$ before, i.e., as the point where $i(x)$ crosses i_p, hence $x_f(H) = (W/2)[2H_p/(H_0 - H)]$, see Eq. (49). The current distribution reads

$$i(x>0) = -\frac{cd}{4\pi\lambda^2} \begin{cases} Hx, & x \leqslant x_i(H_0), \\ Hx - H_0\,[x - x_i(H_0)], & x_i(H_0) \leqslant x \leqslant x_f(H), \\ -H_p\,W/2, & x_f(H) \leqslant x \leqslant x_o(H), \\ -H_p\,W/2 + H\,[x - x_o(H)], & x > x_o(H), \end{cases} \tag{B17}$$

and is analogous to Eq. (B8) with the replacement of $x_s(H) \to x_f(H)$. As the field is reduced, vortices at $x_f(H)$ annihilate with antivortices until $x_f(H) = x_i(H_0)$ and only antivortices are left. As discussed in the main text, this happens for $H = -H_0$. The vortex and current densities for fields $-H_0 \leqslant H \leqslant H_3$ are shown in purple in Fig. 6 and give rise to the magnetic moment (see purple segments in Fig. 7)

$$m(H) = -\frac{dWL}{48\pi}\frac{W^2}{\lambda^2}\left[-\frac{H}{2} + \frac{H}{2}\left(1 + \frac{2H^*}{H}\right)^3 + H_p\left(\frac{2H_p}{H_0 - H}\right)^2 - \frac{H_0}{2}\left(\frac{H_p}{H_0}\right)^3 - \frac{3H_s}{2}\right]. \tag{B18}$$

[1] A. Abrikosov, On the magnetic properties of superconductors of the second group, Zh. Eksp. Teor. Fiz. **32**, 1442 (1957) [Sov. Phys. JETP **5**, 1174 (1957)].

[2] C. P. Bean, Magnetization of hard superconductors, Phys. Rev. Lett. **8**, 250 (1962).

[3] A. I. Larkin and Y. N. Ovchinnikov, Pinning in type-II superconductors, J. Low Temp. Phys. **34**, 409 (1979).

[4] C. P. Bean and J. D. Livingston, Surface barrier in type-II superconductors, Phys. Rev. Lett. **12**, 14 (1964).

[5] J. R. Clem, A model for flux pinning in superconductors, in *Low Temperature Physics-LT 13: Superconductivity*, edited by K. D. Timmerhaus, W. J. O'Sullivan, and E. F. Hammel (Springer US, Boston, 1974), Vol. 3, pp. 102–106.

[6] M. Benkraouda and J. R. Clem, Critical current from surface barriers in type-II superconducting strips, Phys. Rev. B **58**, 15103 (1998).

[7] G. Blatter and V. B. Geshkenbein, Vortex matter, in *Superconductivity: Conventional and Unconventional Superconductors*, edited by K. H. Bennemann and J. B. Ketterson (Springer, Berlin, 2008), pp. 495–637.

[8] E. Zeldov, A. I. Larkin, V. B. Geshkenbein, M. Konczykowski, D. Majer, B. Khaykovich, V. M. Vinokur, and H. Shtrikman, Geometrical barriers in high-temperature superconductors, Phys. Rev. Lett. **73**, 1428 (1994).

[9] M. Benkraouda and J. R. Clem, Magnetic hysteresis from the geometrical barrier in type-II superconducting strips, Phys. Rev. B **53**, 5716 (1996).

[10] E. H. Brandt, Geometric barrier and current string in type-II superconductors obtained from continuum electrodynamics, Phys. Rev. B **59**, 3369 (1999).

[11] J. A. Osborn, Demagnetizing factors of the general ellipsoid, Phys. Rev. **67**, 351 (1945).

[12] E. H. Brandt and M. Indenbom, Type-II-superconductor strip with current in a perpendicular magnetic field, Phys. Rev. B **48**, 12893 (1993).

[13] E. Zeldov, J. R. Clem, M. McElfresh, and M. Darwin, Magnetization and transport currents in thin superconducting films, Phys. Rev. B **49**, 9802 (1994).

[14] A. K. Geim and I. V. Grigorieva, van der Waals heterostructures, Nature (London) **499**, 419 (2013).

[15] K. S. Novoselov, A. Mishchenko, A. Carvalho, and A. H. Castro Neto, 2D materials and van der Waals heterostructures, Science **353**, aac9439 (2016).

[16] Y. Saito, T. Nojima, and Y. Iwasa, Highly crystalline 2D superconductors, Nat. Rev. Mater. **2**, 16094 (2016).

[17] J. M. Lu, O. Zheliuk, I. Leermakers, N. F. Q. Yuan, U. Zeitler, K. T. Law, and J. T. Ye, Evidence for two-dimensional Ising superconductivity in gated MoS_2, Science **350**, 1353 (2015).

[18] X. Xi, Z. Wang, W. Zhao, J.-H. Park, K. T. Law, H. Berger, L. Forró, J. Shan, and K. F. Mak, Ising pairing in superconducting $NbSe_2$ atomic layers, Nat. Phys. **12**, 139 (2016).

[19] Y. Cao, V. Fatemi, S. Fang, K. Watanabe, T. Taniguchi, E. Kaxiras, and P. Jarillo-Herrero, Unconventional superconductivity in magic-angle graphene superlattices, Nature (London) **556**, 43 (2018).

[20] M. Yankowitz, S. Chen, H. Polshyn, Y. Zhang, K. Watanabe, T. Taniguchi, D. Graf, A. F. Young, and C. R. Dean, Tuning superconductivity in twisted bilayer graphene, Science **363**, 1059 (2019).

[21] D. Qiu, C. Gong, S. Wang, M. Zhang, C. Yang, X. Wang, and J. Xiong, Recent advances in 2D superconductors, Adv. Mater. **33**, 2006124 (2021).

[22] S. Das, H. Paudyal, E. R. Margine, D. F. Agterberg, and I. I. Mazin, Electron-phonon coupling and spin fluctuations in the Ising superconductor $NbSe_2$, npj Comput. Mater. **9**, 66 (2023).

[23] L. Balents, C. R. Dean, D. K. Efetov, and A. F. Young, Superconductivity and strong correlations in moiré flat bands, Nat. Phys. **16**, 725 (2020).

[24] J. R. Clem and K. K. Berggren, Geometry-dependent critical currents in superconducting nanocircuits, Phys. Rev. B **84**, 174510 (2011).

[25] M. Rocci, D. Suri, A. Kamra, G. Vilela, Y. Takamura, N. M. Nemes, J. L. Martinez, M. G. Hernandez, and J. S. Moodera, Large enhancement of critical current in superconducting devices by gate voltage, Nano Lett. **21**, 216 (2021).

[26] Z. C. Chen, J. Zhao, F. Gaggioli, S. Grebenchuk, Z. Qiu, Y. Han, J. Hu, K. Watanabe, T. Taniguchi, A. Castro Neto, J. Lu, V. B. Geshkenbein, and K. S. Novoselov, Superconducting transistor and nonreciprocal vortex transport in twisted $NbSe_2$ (unpublished).

[27] D. Y. Vodolazov and F. M. Peeters, Superconducting rectifier based on the asymmetric surface barrier effect, Phys. Rev. B **72**, 172508 (2005).

[28] J. Díez-Mérida, A. Diez-Carlon, S. Y. Yang, Y.-M. Xie, X.-J. Gao, K. Watanabe, T. Taniguchi, X. Lu, A. P. Higginbotham, K. T. Law, and D. K. Efetov, Symmetry-broken Josephson junctions and superconducting diodes in magic-angle twisted bilayer graphene, Nat. Commun. **14**, 2396 (2021).

[29] Y.-Y. Lyu, J. Jiang, Y.-L. Wang, Z.-L. Xiao, S. Dong, Q.-H. Chen, M. V. Milošević, H. Wang, R. Divan, J. E. Pearson *et al.*, Superconducting diode effect via conformal-mapped nanoholes, Nat. Commun. **12**, 2703 (2021).

[30] B. Pal, A. Chakraborty, P. K. Sivakumar, M. Davydova, A. K. Gopi, A. K. Pandeya, J. A. Krieger, Y. Zhang, M. Date, S. Ju, N. Yuan *et al.*, Josephson diode effect from cooper pair momentum in a topological semimetal, Nat. Phys. **18**, 1228 (2022).

[31] C. Baumgartner, L. Fuchs, A. Costa, S. Reinhardt, S. Gronin, G. C. Gardner, T. Lindemann, M. J. Manfra, P. E. Faria Junior, D. Kochan *et al.*, Supercurrent rectification and magnetochiral effects in symmetric Josephson junctions, Nat. Nanotechnol. **17**, 39 (2022).

[32] L. Bauriedl, C. Bäuml, L. Fuchs, C. Baumgartner, N. Paulik, J. M. Bauer, K.-Q. Lin, J. M. Lupton, T. Taniguchi, K. Watanabe *et al.*, Supercurrent diode effect and magnetochiral anisotropy in few-layer $NbSe_2$, Nat. Commun. **13**, 4266 (2022).

[33] T. Golod and V. M. Krasnov, Demonstration of a superconducting diode-with-memory, operational at zero magnetic field with switchable nonreciprocity, Nat. Commun. **13**, 3658 (2022).

[34] Y. V. Fominov and D. S. Mikhailov, Asymmetric higher-harmonic squid as a Josephson diode, Phys. Rev. B **106**, 134514 (2022).

[35] J.-X. Lin, P. Siriviboon, H. D. Scammell, S. Liu, D. Rhodes, K. Watanabe, T. Taniguchi, J. Hone, M. S. Scheurer, and J. I. A. Li, Zero-field superconducting diode effect in small-twist-angle trilayer graphene, Nat. Phys. **18**, 1221 (2022).

[36] D. Suri, A. Kamra, T. N. G. Meier, M. Kronseder, W. Belzig, C. H. Back, and C. Strunk, Non-reciprocity of vortex-limited critical current in conventional superconducting micro-bridges, Appl. Phys. Lett. **121**, 102601 (2022).

[37] A. Gutfreund, H. Matsuki, V. Plastovets, A. Noah, L. Gorzawski, N. Fridman, G. Yang, A. Buzdin, O. Millo, J. W. A. Robinson, and Y. Anahory, Direct observation of a superconducting vortex diode, Nat. Commun. **14**, 1630 (2023).

[38] D. Margineda, A. Crippa, E. Strambini, Y. Fukaya, M. T. Mercaldo, M. Cuoco, and F. Giazotto, Sign reversal diode effect in superconducting Dayem nanobridges, Nat. Commun. **6**, 343 (2023).

[39] A. Sundaresh, J. I. Väyrynen, Y. Lyanda-Geller, and L. P. Rokhinson, Diamagnetic mechanism of critical current nonreciprocity in multilayered superconductors, Nat. Commun. **14**, 1628 (2023).

[40] Y. Hou, F. Nichele, H. Chi, A. Lodesani, Y. Wu, M. F. Ritter, D. Z. Haxell, M. Davydova, S. Ilić, O. Glezakou-Elbert, A. Varambally, F. S. Bergeret, A. Kamra, L. Fu, P. A. Lee, and J. S. Moodera, Ubiquitous superconducting diode effect in superconductor thin films, Phys. Rev. Lett. **131**, 027001 (2023).

[41] F. Paolucci, G. De Simoni, and F. Giazotto, A gate- and flux-controlled supercurrent diode effect, Appl. Phys. Lett. **122**, 042601 (2023).

[42] K. Nakamura, A. Daido, and Y. Yanase, Orbital effect on intrinsic superconducting diode effect, Phys. Rev. B. **109**, 09450 (2024).

[43] M. Nadeem, M. S. Fuhrer, and X. Wang, The superconducting diode effect, Nat. Rev. Phys. **5**, 558 (2023).

[44] G. W. Swan, Current distribution in a thin superconducting strip, J. Math. Phys. **9**, 1308 (1968).

[45] R. P. Huebener, R. T. Kampwirth, and J. R. Clem, Meissner shielding currents and magnetic flux penetration in thin-film superconductors, J. Low Temp. Phys. **6**, 275 (1972).

[46] J. Pearl, Current distribution in superconducting films carrying quantized fluxoids, Appl. Phys. Lett. **5**, 65 (1964).

[47] V. Shmidt and G. Mkrtchyan, Vortices in type-ll superconductors, Sov. Phys. Usp. **17**, 170 (1974).

[48] G. Stejic, A. Gurevich, E. Kadyrov, D. Christen, R. Joynt, and D. C. Larbalestier, Effect of geometry on the critical currents of thin films, Phys. Rev. B **49**, 1274 (1994).

[49] G. M. Maksimova, Mixed state and critical current in narrow semiconducting films, Fiz. Tverd. Tela (St. Petersburg) **40**, 1773 (1998) [Phys. Solid State **40**, 1607 (1998)].

[50] B. L. T. Plourde, D. J. Van Harlingen, D. Y. Vodolazov, R. Besseling, M. B. S. Hesselberth, and P. H. Kes, Influence of edge barriers on vortex dynamics in thin weak-pinning superconducting strips, Phys. Rev. B **64**, 014503 (2001).

[51] A. Larkin and Y. N. Ovchinnikov, Influence of inhomogeneities on superconductor properties, Zh. Eksp. Teor. Fiz. **61**, 1221 (1971) [Sov. Phys. JETP **34**, 651 (1972)].

[52] M. Tinkham, *Introduction to Superconductivity*, Dover Books on Physics Series (Dover Publications, New York, 2004).

[53] K. Xu, P. Cao, and J. R. Heath, Achieving the theoretical depairing current limit in superconducting nanomesh films, Nano Lett. **10**, 4206 (2010).

[54] G. P. Mikitik, Critical current in thin flat superconductors with Bean-Livingston and geometrical barriers, Phys. Rev. B **104**, 094526 (2021).

[55] J. Villegas, S. Savel'ev, F. Nori, E. Gonzalez, J. Anguita, R. García, and J. Vicent, A superconducting reversible rectifier that controls the motion of magnetic flux quanta, Science **302**, 1188 (2003).

[56] C. de Souza Silva, J. Van de Vondel, M. Morelle, and V. Moshchalkov, Controlled multiple reversals of a ratchet effect, Nature (London) **440**, 651 (2006).

[57] W. Gillijns, A. V. Silhanek, V. V. Moshchalkov, C. J. O. Reichhardt, and C. Reichhardt, Origin of reversed vortex ratchet motion, Phys. Rev. Lett. **99**, 247002 (2007).

[58] W. Lang, Nanostructured superconductors, in *Encyclopedia of Condensed Matter Physics*, 2nd ed., edited by T. Chakraborty (Academic Press, Oxford, 2024), pp. 368–380.

[59] S. Hoshino, R. Wakatsuki, K. Hamamoto, and N. Nagaosa, Nonreciprocal charge transport in two-dimensional noncentrosymmetric superconductors, Phys. Rev. B **98**, 054510 (2018).

[60] F. Ando, Y. Miyasaka, T. Li, J. Ishizuka, T. Arakawa, Y. Shiota, T. Moriyama, Y. Yanase, and T. Ono, Observation of superconducting diode effect, Nature (London) **584**, 373 (2020).

[61] A. Daido, Y. Ikeda, and Y. Yanase, Intrinsic superconducting diode effect, Phys. Rev. Lett. **128**, 037001 (2022).

[62] N. F. Q. Yuan and L. Fu, Supercurrent diode effect and finite-momentum superconductors, Proc. Natl. Acad. Sci. USA **119**, e2119548119 (2022).

[63] B. Zinkl, K. Hamamoto, and M. Sigrist, Symmetry conditions for the superconducting diode effect in chiral superconductors, Phys. Rev. Res. **4**, 033167 (2022).

[64] P. J. W. Moll and V. B. Geshkenbein, Evolution of superconducting diodes, Nat. Phys. **19**, 1379 (2023).

[65] A. He, C. Xue, and Y.-H. Zhou, Switchable reversal of vortex ratchet with dynamic pinning landscape, Appl. Phys. Lett. **115**, 032602 (2019).

[66] T. Ideue, S. Koshikawa, H. Namiki, T. Sasagawa, and Y. Iwasa, Giant nonreciprocal magnetotransport in bulk trigonal superconductor $PbTaSe_2$, Phys. Rev. Res. **2**, 042046(R) (2020).

[67] J. Jiang, Y.-L. Wang, M. V. Milošević, Z.-L. Xiao, F. M. Peeters, and Q.-H. Chen, Reversible ratchet effects in a narrow superconducting ring, Phys. Rev. B **103**, 014502 (2021).

[68] L. Embon, Y. Anahory, A. Suhov, D. Halbertal, J. Cuppens, A. Yakovenko, A. Uri, Y. Myasoedov, M. L. Rappaport, M. E. Huber *et al.*, Probing dynamics and pinning of single vortices in superconductors at nanometer scales, Sci. Rep. **5**, 7598 (2015).

[69] E. H. Brandt, Electric field in superconductors with rectangular cross section, Phys. Rev. B **52**, 15442 (1995).

[70] G. P. Mikitik and E. H. Brandt, Critical state in thin anisotropic superconductors of arbitrary shape, Phys. Rev. B **62**, 6800 (2000).

[71] Y. Anahory, J. Reiner, L. Embon, D. Halbertal, A. Yakovenko, Y. Myasoedov, M. L. Rappaport, M. E. Huber, and E. Zeldov, Three-junction squid-on-tip with tunable in-plane and out-of-plane magnetic field sensitivity, Nano Lett. **14**, 6481 (2014).

[72] S. Grover, M. Bocarsly, A. Uri, P. Stepanov, G. Di Battista, I. Roy, J. Xiao, A. Y. Meltzer, Y. Myasoedov, K. Pareek *et al.*, Chern mosaic and Berry-curvature magnetism in magic-angle graphene, Nat. Phys. **18**, 885 (2022).